Research Square

Preprints are preliminary reports that have not undergone peer review.
They should not be considered conclusive, used to inform clinical practice,
or referenced by the media as validated information.

Programming Energy–Bio Interfaces through Ligand-Directed Electronic Transport in Atomically Precise Gold Nanoclusters

Rohit Sharma

rohitksg@pu.ac.in

Panjab University

Soumen Dubey
Suman Mondal
Kajal gupta
Kalyani Iswar
Rathindranath Biswas
Pritha Chakraborty
Suprabhat Mukherjee
Pratip Chakraborty
Aravind Kumar Rengan

Department of Biomedical Engineering Indian Institute of Technology Hyderabad Hyderabad Telangana India

Kalisadhan Mukherjee

Article

Keywords: Ligand engineering, NIR-emitting gold nanoclusters, Exciton coupling, Interfacial charge transfer, Hydrogen evolution reaction, Reactive oxygen species, Cancer nano-theranostics

Posted Date: August 12th, 2026

DOI: https://doi.org/10.21203/rs.3.rs-10508579/v1

License: This work is licensed under a Creative Commons Attribution 4.0 International License.
Read Full License

Additional Declarations: There is **NO** Competing Interest.

Programming Energy–Bio Interfaces through Ligand-Directed Electronic Transport in Atomically Precise Gold Nanoclusters

Soumen K. Dubey[1], Suman Mondal[2], Kajal Gupta[3], Kalyani Iswar[4], Rathindranath Biswas[5], Pritha Chakraborty[6], Aravind Kumar Rengan[4], Suprabhat Mukherjee[6], Pratip Chakraborty[7,8], Kalisadhan Mukherjee[2*], and Rohit K. Sharma[1*]

[1] Department of Chemistry & Centre of Advanced Studies, Panjab University, Chandigarh-160014, India *Email: rohitksg@pu.ac.in

[2] Department of Chemistry, Pandit Deendayal Energy University, Gandhinagar-382426, Gujarat, India

[3] Department of Chemistry, Nistarini College, Purulia-723101, West Bengal, India

[4] Department of Biomedical Engineering, Indian Institute of Technology Hyderabad, Kandi-502284, Telangana, India

[5] Department of Chemistry, Indian Institute of Technology Bombay, Powai-400076, Mumbai, India

[6] Integrative Biochemistry & Immunology Laboratory (IBIL), Department of Animal Science, Kazi Nazrul University, Asansol-713340, West Bengal, India

[7] Cradle Fertility Centre, 496/1, Diamond Park, Joka, Kolkata 700104, West Bengal, India

[8] Assisted Reproduction Technology Division, Institute of Reproductive Medicine, Salt Lake City, Kolkata-700106, West Bengal, India

Abstract

Engineering multifunctional nano-systems with programmable electronic transport remains a fundamental challenge for integrating optical, catalytic, and biomedical functions within a single nanomaterial. Herein, a new aromatic-amide functionalized chiral small ligand, (R)-5-(1,2-dithiolan-3-yl)-N-(napthalen-1-yl)-pentanamide (NDLA), has been synthesized to construct atomically precise gold nanoclusters (NDLA-AuNCs) with tailored electronic and interfacial properties. The resulting NDLA-AuNCs exhibit near-infrared emission (800-1200 nm), pronounced exciton-coupled circular dichroism, and intrinsic semiconducting behaviour governed by a correlated barrier hopping mechanism, with a Mott temperature of 1.4×10^6 K, localization length of 0.3 nm, and density of states at fermi level of 4.9×10^{21} states$\cdot$ $eV^{-1}\cdot$ cm^{-3}, demonstrating ligand-directed chirality transfer and charge migration through localized electronic states. The resulting electronic architecture promotes rapid interfacial charge transfer that drives superior electrocatalytic hydrogen evolution compared with reported bare AuNCs. In a biological environment, the same charge-transport dynamics drive ROS generation under dark and light, inducing mitochondrial dysfunction and potent triple-negative breast cancer cytotoxicity, while preserving excellent in vitro and in vivo biocompatibility. By directly correlating ligand chemistry with electronic transport, this work establishes electronic structure engineering as a proof-of-concept for programming multifunctionality in nanoscale materials and provides an integrated "energy-bio interface" framework for designing next-generation catalytic and therapeutic nano-systems.

Keywords: Ligand engineering**,** NIR-emitting gold nanoclusters; Exciton coupling; Interfacial charge transfer; Hydrogen evolution reaction; Reactive oxygen species; Cancer nano-theranostics

1. Introduction

The convergence of nanotechnology with sustainable energy production and precision biomedicine has become a promising frontier representing a new opportunity to address multiple interconnected global challenges through a unified material platform.[1–4] In this context, metal nanoclusters (MNCs) with precise atomic structures have gained significant attention as an exceptional nanomaterial that bridges the gap between individual atoms and larger nanoparticles.[5–7] Recent progress in synthetic control and atomic-scale characterization has revealed that the discrete electronic energy levels of MNCs produce highly structure-dependent physicochemical properties, permitting broad functionality across the

catalytic energy conversion and biomedical applications.[8,9] However, among the MNCs derived from transition, noble and coinage metals, gold nanoclusters (AuNCs) have emerged as promising candidates for translational applications, owing to their exceptional chemical stability, biological compatibility, and catalytic versatility.[10–13]

The versatility of noble metal-based nanomaterials in catalysis is particularly significant in the context of sustainable energy production, as the catalytic activity plays a central role in enhancing the efficient conversion of renewable energy through electrocatalytic pathways.[14,15] The development of high-performance catalysts with optimized active sites and long-term durability under experimental conditions critically depends on the electronic structure and interfacial charge-transfer kinetics of the catalyst.[16,17] The atomically precise AuNCs with size-dependent electronic structures offer a powerful handle to finely tune the hydrogen free energy (ΔG_H^*) towards thermoneutral values, while facilitating efficient electron transfer across the catalyst-electrolyte interface.[18] This optimization of adsorption energy and charge transport capability is essential for accelerating the hydrogen evolution reaction (HER) during water electrolysis. These properties lead such materials to emerge as highly promising electrocatalysts for efficient and scalable hydrogen production. Beyond energy production, the same atomic precision and tunable electronic properties also provide additional functionalities. Further, the ultrasmall size (< 2 nm), strong near-infrared (NIR) absorption/ emission, and controlled surface modification allow their applications in deep-tissue imaging, photothermal or photodynamic therapy (PTT/ PDT), and reactive oxygen species (ROS) modulation.[19] Their ultrasmall size reduces long-term organ accumulation via renal clearance and potential toxicity associated with larger nanomaterials, making them suitable for *in vivo* applications. In addition, the high surface-to-volume ratio of the AuNCs facilitates tunable surface functionalization with targeting ligands, peptides, antibodies, or drug molecules for targeted drug delivery and theranostic platforms. These nanomaterials are particularly significant because of their NIR photoactivity in biotherapy and their ability to control ROS generation for inducing selective apoptosis or ferroptosis in targeted diseases.[20–22] Conversely, in the context of cyto-protection and anti-inflammatory purposes, the surface chemistry of AuNCs can also be engineered to scavenge excess ROS for treating neurogenerative diseases, ischemic injury, and inflammatory disorders.[23,24] This dual functionality to amplify or quench ROS highly depends on the design and surface functionalization of the nanoclusters and underscores remarkable therapeutic versality of these ultrasmall AuNCs for next-generation nanomedicine.[25]

Although catalytic and biological activities may appear to address different objectives, the underlying physicochemical processes, such as charge transfer, surface reactivity and light-matter interactions, are fundamentally similar in both applications.[26–28] The aforementioned processes enable absorption, activation, and conversion of reactant species in catalysis, whereas the interfacial electron transfer plays a crucial role in enzyme activation, photosynthetic and redox signalling pathways in a biological system. These shared mechanisms establish a conceptual bridge between energy production and biomedicine, thereby facilitating the development of a multifunctional nanocluster platform. Despite these complementary advantages, the existing studies on metal based nanomaterials typically focus on either catalysis or biomedical applications, and have rarely been integrate both areas within a single entity.[29–33] One of the major challenges in combining these functional attributes depends on the nature of surface ligands present in the metal based nanoclusters, as well as their design strategy. In most biomedical applications, specifically AuNCs are usually capped with peptides, proteins, or other biopolymers to improve biocompatibility and enhance target-specific binding with biological molecules.[34–36] However, these large and flexible ligands can block catalytic sites and hinder the electron transfer processes, which reduces their effectiveness in electrochemical applications.[37,38] Conversely, the AuNCs employed in catalysis are typically stabilized with small thiol or phosphine-containing ligands. These smaller ligands facilitate better electron transfer and maintain catalytically accessible sites, but are unable to provide the biomolecular recognition for selective therapeutic applications. Consequently, achieving a balance between catalytic efficiency and biological functionality of ligand-stabilized nanomaterial remains a major challenge.[39]

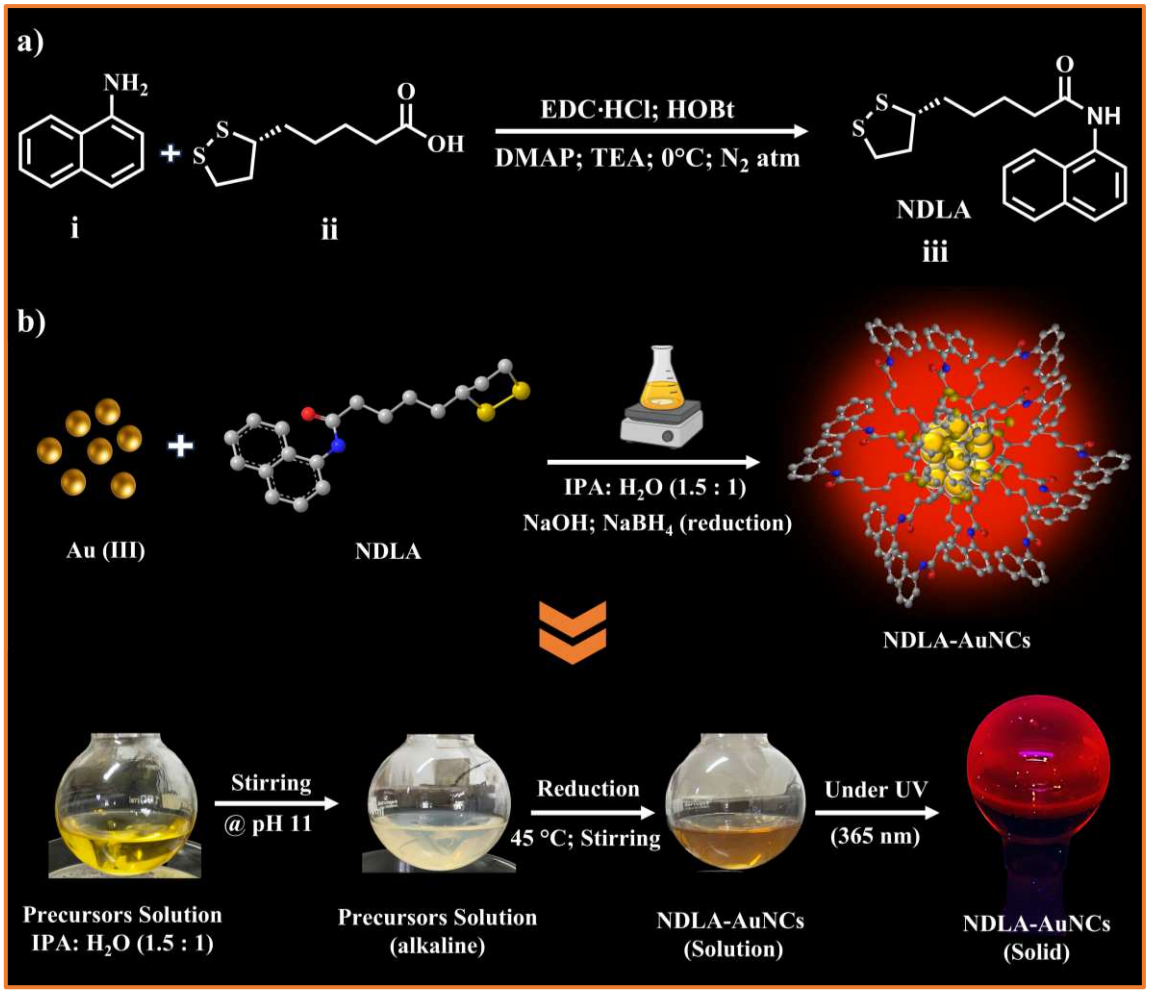
The present study intends to overcome these limitations by adopting an alternative strategy, called ‘integration by design.’ Instead of combining multiple components with different functions, the currently proposed methodology is based the integration of both catalytic and therapeutic functions directly into a single material. To address this, a small organic ligand, containing an aromatic-amide structure with a chiral anchoring group, was considered as a better alternative to conventional peptidic and biomolecular ligands.[40–43] In this design strategy, the amide group provides hydrogen bonding and maintains hydrophilic balance, which supports selective interaction with biomolecular targets. The aromatic framework tends to improve NIR photophysical properties through extended delocalization. In addition, the small size of the ligand reduces tunnelling or hopping barriers for electron transfer, enabling efficient electrochemical and biological redox processes.[44,45] Furthermore, the introduction

of chirality in the ligand design provides an additional control over both domains. In catalysis, a chiral surface can modulate the adsorption geometry and binding energies of the reaction intermediates, thereby influencing the reaction kinetics and selectivity.[46,47] While in biomedicine, the same chiral environment can promote enantioselective recognition of biomolecules and improve cellular uptake through stereospecific interactions.[48,49]

Keeping in mind the importance of ligand structure, this study presents the synthesis of a newly designed aromatic, dithiolane functionalized chiral (R)-5-(1,2-dithiolan-3-yl)-N-(napthalen-1-yl)-pentanamide (abbreviated as NDLA) ligand capped AuNCs to explore their potential applicability across the interdisciplinary field. The distinctive structural features of this material exhibit exceptional multifunctionality, such as NIR photoluminescence, exciton coupling-assisted chiroptical property, electrical semi-conductivity, redox activity, efficient electrocatalytic HER, and ROS-mediated anticancer properties. To the best of our knowledge, this study represents the first report of a direct "energy-bio interface" material in which catalytic hydrogen production and biological activities are intrinsically coupled through a common electronic structure and interfacial charge transfer pathways, rather than independently engineered.

2. Result and Discussion:

Atomically precise gold nanoclusters (AuNCs) are fundamentally governed by their ligand framework to achieve atomic-level precision and provide tunable functional properties. [35] Beyond providing structural control, the ligand environment tends to stabilize the nucleation process and influence the relationship between photophysical and electronic properties, both of which factors are essential for achieving application-specific performance. [44,45] In this study, a new aromatic chiral NDLA ligand has been synthesized **[Scheme 1(a)]** and characterized using NMR and mass spectrometry **[Figure S1-S3]**. This ligand framework was intentionally designed as it exhibited a distinctive tripartite molecular structure that synergistically combines multiple functional elements i.e. (i) a stereo-chemically defined (R)-lipoic acid derived bidentate 1,2-dithiolane moiety that anchors to the curved and atomically discrete surface of the gold core; (ii) a conformationally flexible pentyl spacer chain that provides optimal geometric positioning and dynamic adaptability during cluster assembly; and (iii) an electron-rich naphthalene group which covalently linked through an amide bond that imparts both electronic modulation and potential intermolecular π-π stacking capabilities.



Scheme 1: Scheme for (a) chemical synthesis of NDLA ligand, (b) synthesis of gold nanoclusters (NDLA-AuNCs) with a pictorial representation outlining stepwise synthetic procedure.

Following the synthesis of chiral NDLA ligand, the atomically precise AuNCs were synthesized via a NaOH-mediated $NaBH_4$ reduction method using isopropanol-water (1.5:1) solvent system **[Scheme 1(b)]**. The formation of these NDLA-AuNCs were subsequently confirmed using high-resolution transmission electron microscopy (HRTEM) analysis which revealed well-dispersed nanoclusters with an average core diameter of 1.17 ± 0.22 nm, indicating the formation of uniform and well-dispersed nanostructures **[Figure 1(a-b) & S4]**. Complementary dynamic light scattering (DLS) measurements showed a single narrow peak, having an average hydrodynamic diameter of 4.1 nm, which confirmed the presence of surface ligands and the surrounding solvent layer [**Figure S5]**. This ultrasmall size, along with the colloidal stability of AuNCs is well known to facilitate their clinical translation by enabling rapid renal clearance and preventing bioaccumulation in organs, thereby enhancing their suitability as molecular probes in biomedical applications, particularly in diagnostic imaging.[50,51]

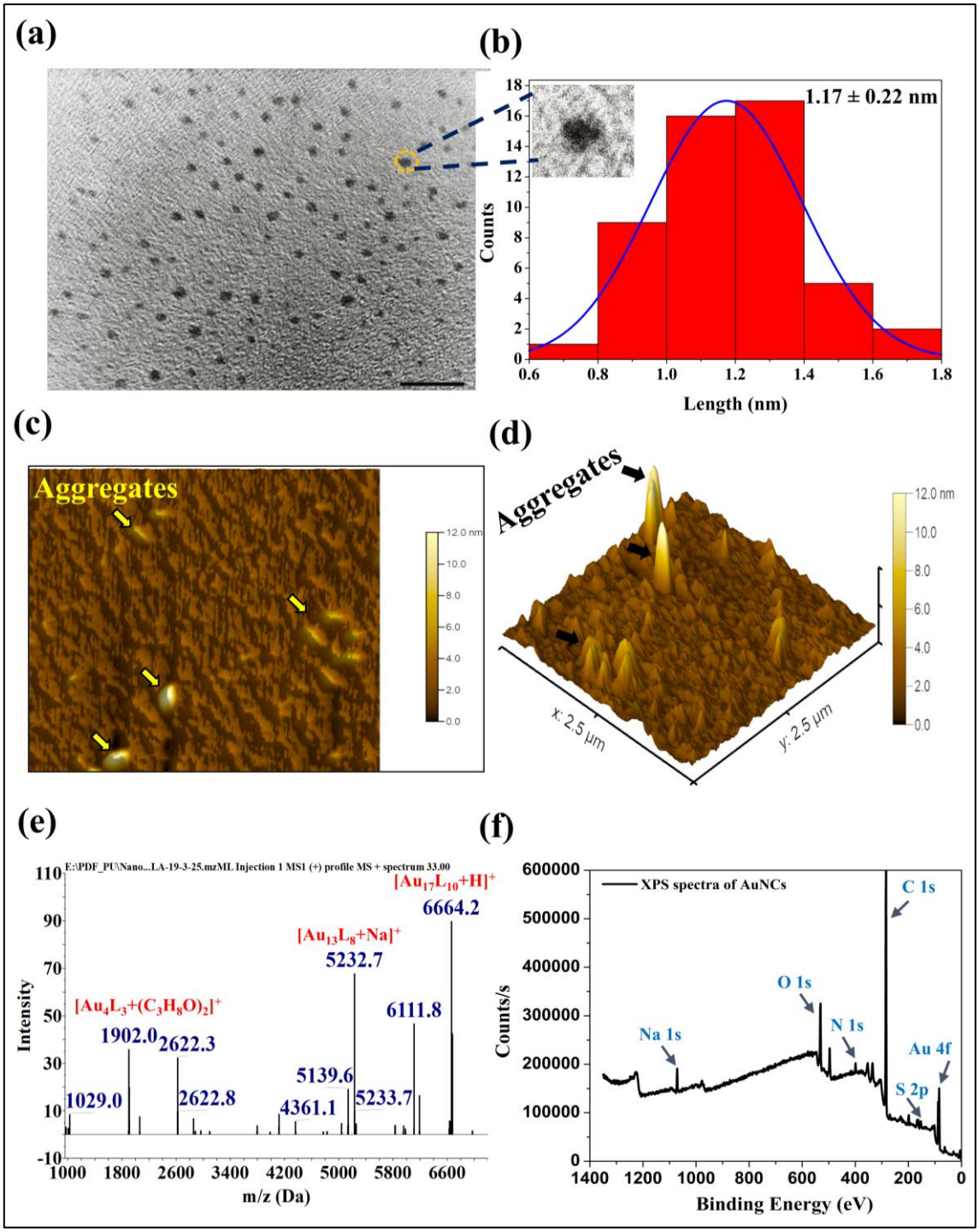


Figure 1. (a) High-resolution TEM (HRTEM) image of NDLA-AuNCs (scale 10 nm); (b) Size distribution histogram of NDLA-AuNCs derived from HRTEM analysis; (c) AFM analysis of NDLA-AuNCs (yellow colour arrow depicts aggregated AuNCs during deposition); (d) 3D- topographic image of NDLA-AuNCs showing multiple nanospikes like morphology (scale 2.5 × 2.5 µm²); (e) ESI-MS spectrum of NDLA-AuNCs recorded in positive-ion mode; (f) Survey XPS spectra of NDLA-AuNCs

Further, the surface morphology and height distribution of the NDLA-AuNCs were evaluated using atomic force microscopy (AFM) analysis **[Figure 1(c)],** in which the three-dimensional topographic image, recorded over a 2.5 × 2.5 µm² area, revealed a discrete nanoscale spike-

like island **[Figure 1(c-d)]**. The statistical analysis of the topographic data yielded an average cluster height of 2.43 nm [**Figure S6 & Table S1]**. Notably, the high degree of dispersity and the presence of isolated nano-spikes can directly modulate the functional performance of the AuNCs across catalysis, sensing, and biomedical applications.[52,53] To assess the homogeneity and structural integrity of the NDLA-AuNCs, the native polyacrylamide gel electrophoresis (PAGE) analysis was performed, which revealed a single, well-defined band, indicating that these nanoclusters existed as a homogeneous and intact species under non-denaturing conditions **(Figure S7)**. In contrast, electrospray ionization mass spectrometry (ESI-MS) analysis showed the dominant monoisotopic peak at m/z 6664.17 Da, corresponding to the intact singly charged $[Au_{17}L_{10}]^+$ nanoclusters (theo. Mass 6664.42 Da), several lower intensity peaks assigned to smaller gold-ligand fragments such as $[Au_{13}L_8+Na]^+$ and $[Au_4L_3+(C_3H_8O)_2]^+$ **[Figure 1(e)]**. These fragments can be attributed to gas-phase fragmentation during the electrospray ionization process.

Similarly, the structural properties of the newly synthesized ligand (NDLA) and the ligand-metal coordination environment were analyzed by using Fourier-transform infrared (FTIR) spectroscopy **[Figure S8]**. The prominent absorption bands of N–H stretching at 3298 cm^{-1} confirmed the presence of amide functionalities within the ligand and nanoclusters system. The strong absorption at 1645 cm^{-1} corresponds to the amide-I (C=O stretching) band, and the complementary amide-II (N–H bending or C–N stretching) band at 1553 cm^{-1} provides additional confirmation of the amide linkage. The C–N stretching vibration at 1252 cm^{-1} also confirmed the presence of the amide functional group. Notably, a clear peak at 644 cm^{-1} corresponded to the S–S stretching vibration of the disulfide bond present in the (R)-lipoic acid moiety **[Figure S8 (inset)]**. Following the synthesis of AuNCs, this characteristic disulfide peak completely disappeared, which directly provides the spectroscopic evidence for the formation of Au–S coordination bond.

The X-ray photoelectron spectroscopic (XPS) analysis was performed to investigate the oxidation states of the NDLA-AuNCs system, and confirmed the presence of Au, S, C, N, and O elements **[Figure 1(f)]**. The Au 4f spectrum depicted two characteristic peaks at 84.34 eV (Au $4f_{7/2}$) and 88.05 eV (Au $4f_{5/2}$), with a spin-orbit splitting of 3.71 eV. Further, the deconvolution of the Au spectrum indicated the contribution from both Au (0) and Au (I) oxidation states **[Figure 2(a)]**. This analysis suggested that a core-shell electronic structure has been formed during the synthesis of AuNCs. The additional photoelectron peaks were observed at 162.53 eV (S $2p_{3/2}$), 284.58 eV (C 1s), 399.7 eV (N 1s), and 531.71 eV (O 1s), which corresponded to the elements present in the ligand structure **[Figure S10]**. The peak at 162.93

eV indicated the presence of thio-protected gold surfaces. The C 1s peak at 284.58 eV is characteristic of sp^2 hybridized carbon atoms in the aromatic rings**.** The N 1s (399.7 eV) and O 1s (531.70 eV) peaks confirmed the amide groups within the ligand structure. Additionally, the presence of Au, S, C, N, and O in the bulk sample was verified using energy-dispersive X-ray spectroscopy (EDS) and elemental mapping analysis **[Figure S(11-12)]**. The EDS spectrum exhibited peaks at 2.12 keV and at 9.71 keV, which corresponded to the Mα1 and Lα1 signals of elemental gold. The elemental sulphur was identified by its characteristic kα peak at 2.31 keV. Additionally, the presence of carbon, oxygen, and nitrogen was detected with signals observed at 0.28 keV, 0.52 keV, and 0.39 keV, respectively.

The morphological nature of the NDLA-AuNCs along with NDLA ligand was further analyzed using powder X-ray diffraction (PXRD) in which the presence of intense and well-defined diffraction peaks of the NDLA-ligand in the 2θ range of 10° to 25° indicated a high degree of structural ordering within the ligand system **[Figure 2(b)]**. The selected area electron diffraction (SAED) pattern of NDLA-AuNCs exhibited a combination of distinct bright diffraction spots and concentric rings, which are characteristic of nanocrystalline materials with partially ordered domains **[Figure 2(c)]**. The observed diffraction rings were indexed to the (111), (200), (220), and (311) lattice of the face-centred cubic structure of Au. The PXRD pattern of the AuNCs depicted peaks at the 2θ values of ~38.22 (111), ~44.58 (200), ~64.79 (220), ~77.98 (311), and ~81.7 (222), which were associated with the cubic crystalline nature of gold (JCPDS no. 04-0784) **[Figure 2(d)]**.

The electronic and chiroptical properties of synthesized NDLA-AuNCs were further explored, in which the UV-vis spectrum from 200-800 nm of the nanoclusters revealed the absence of a broad surface plasmon resonance band near 540-560 nm **[Figure 2(e)]**. This validated the atomically precise nature of the nanoclusters, although the presence of a band at 290 nm revealed that the aromatic ligands were successfully bound with the nanocluster system and displayed π-π* transition. The fluorescence emission spectrum displayed a prominent NIR emission peak from 800-1200 nm, centered at 935 nm upon excitation at 690 nm, which is attributed to ligand to metal charge transfer and inter-band transitions within the confined gold core **[Figure 2(f)]**. This emission profile strategically bridges the NIR-I (780-950 nm) and NIR-II (1000-1700 nm) biological transparency windows, thereby presenting this nanocluster as a possible versatile dual-region optical imaging agent. The NIR-II overlap offers significant advantages for deep-tissue bioimaging because it allows light to penetrate tissues more effectively and reduces interference from autofluorescence in biological samples.[54,55]

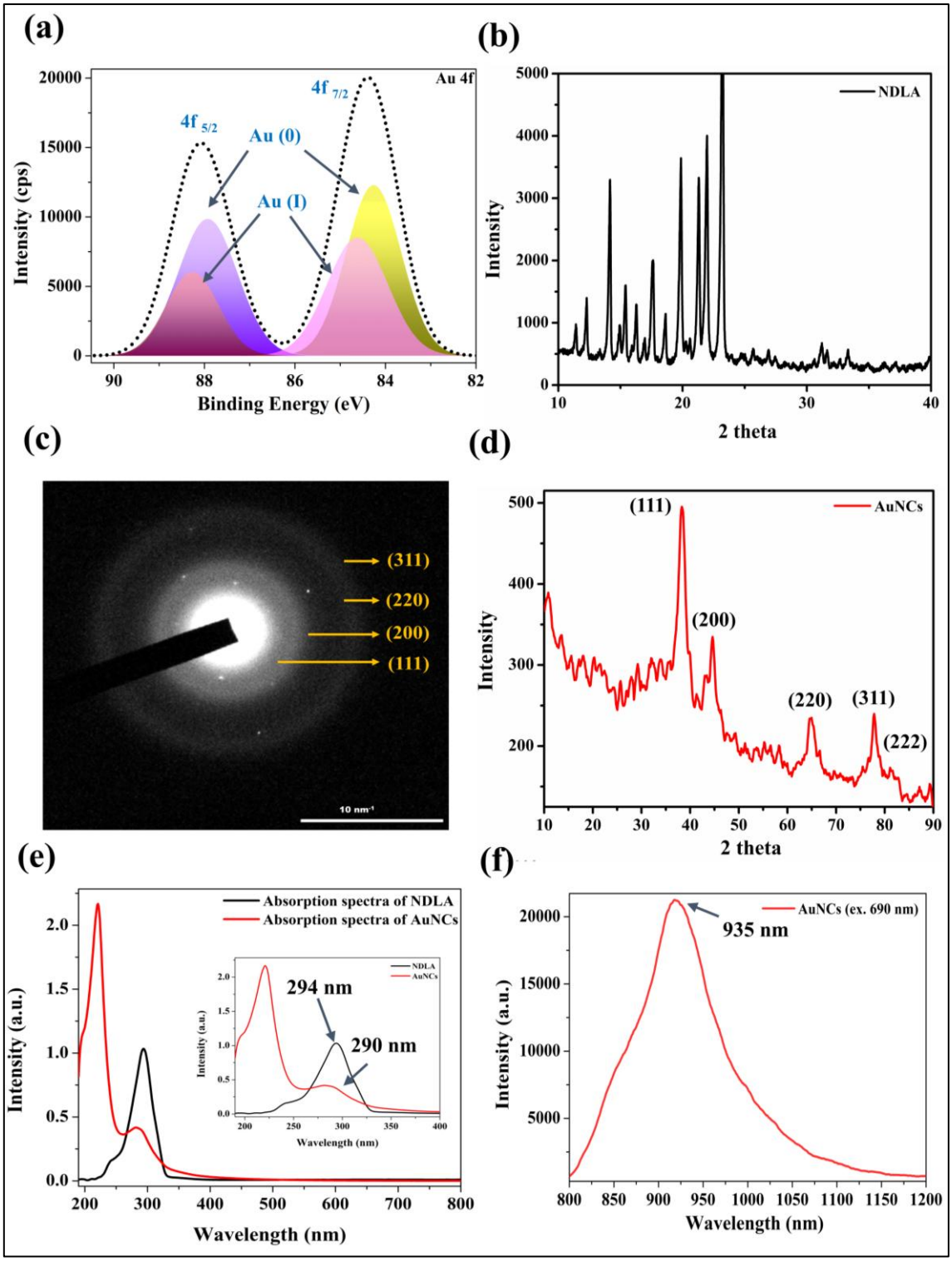


Figure 2. (a) XPS spectra of deconvoluted gold (Au) 4f region of NDLA-AuNCs; (b) SAED pattern of NDLA-AuNCs displaying ring-like features consistent with the FCC lattice of gold; (c) PXRD pattern of ligand NDLA; (d) PXRD pattern of NDLA-AuNCs ; (e) UV-vis absorption spectra of NDLA ligand and NDLA-AuNCs ; (f) Photoluminescence spectra of NDLA-AuNCs upon excitation at 690 nm, collected using an 800 nm long band pass filter.

The chiroptical properties of both the ligand (NDLA) and the NDLA-AuNCs were analyzed using circular dichroism (CD) spectroscopy. The ligand alone exhibited typical chiral signals,

including negative peaks around 208 nm and 234 nm, a positive peak near 275 nm, and a weak negative band near 330 nm arising from its inherent chiral electronic transitions **[Figure 3(a)]**. After the formation of nanoclusters, the AuNCs demonstrated different CD features, including an intense band near 220 nm, a strong positive signal around 265 nm, a clear negative band near 330 nm, and a chiral signal extending to about 430 nm **[Figure 3(b)]**. These changes in the spectrum suggest that the ligand structure rearranges after binding to the nanocluster, thereby transferring its molecular chirality to the AuNCs core. This ligand-induced chirality for the nanocluster framework concurs with the previously reported chiral AuNCs systems.[54] Therefore, the relevance of ligand structure is crucial for overall stability and chirality of AuNCs, as the ligand not only leads to stabilization of nanoclusters but also tends to impose a chiral environment on the AuNCs system.

The spectral analysis of the AuNCs was systematically investigated using a combined CD and UV-vis spectroscopic approach to better understand whether the CD signals arise from individual molecular electronic transitions (monomeric transitions) or from interactions between multiple electronic states (excitonically coupled states). The CD spectrum displayed a bi-signate signal with a zero crossing at 294 nm, which closely overlapped with the exciton absorption wavelength of the ligand and AuNCs system, with a calculated exciton coupling constant (J) of 0.48 eV **[Figure 3(c)]**. The appearance of such bi-signate CD couplet clearly indicated that the exciton coupling occurs between the adjacent clusters, spatially well separated by the chiral ligand shell.[55,56] This finding is especially significant for several key implications, as firstly it follows the condition for Frenkel exciton coupling, which include degenerate transition energies, sufficient dipole-dipole interaction, and atomic-level uniformity.[57,58] These conditions tend to avoid the spectral broadening as typically observed for conventional nanoparticles. Secondly, the zero-crossing feature also provides direct insight into the structural framework of nanoclusters, where the sign of the couplet reflects the helical arrangements of the ligands.[59,60] Finally, and more broadly, these findings establish a much-needed pathway for rational engineering of ligand-shell framework leading into tailored functionalities including light harvesting, chiroptical sensing and quantum photonic probe at the sub-2nm scale.[61–63]

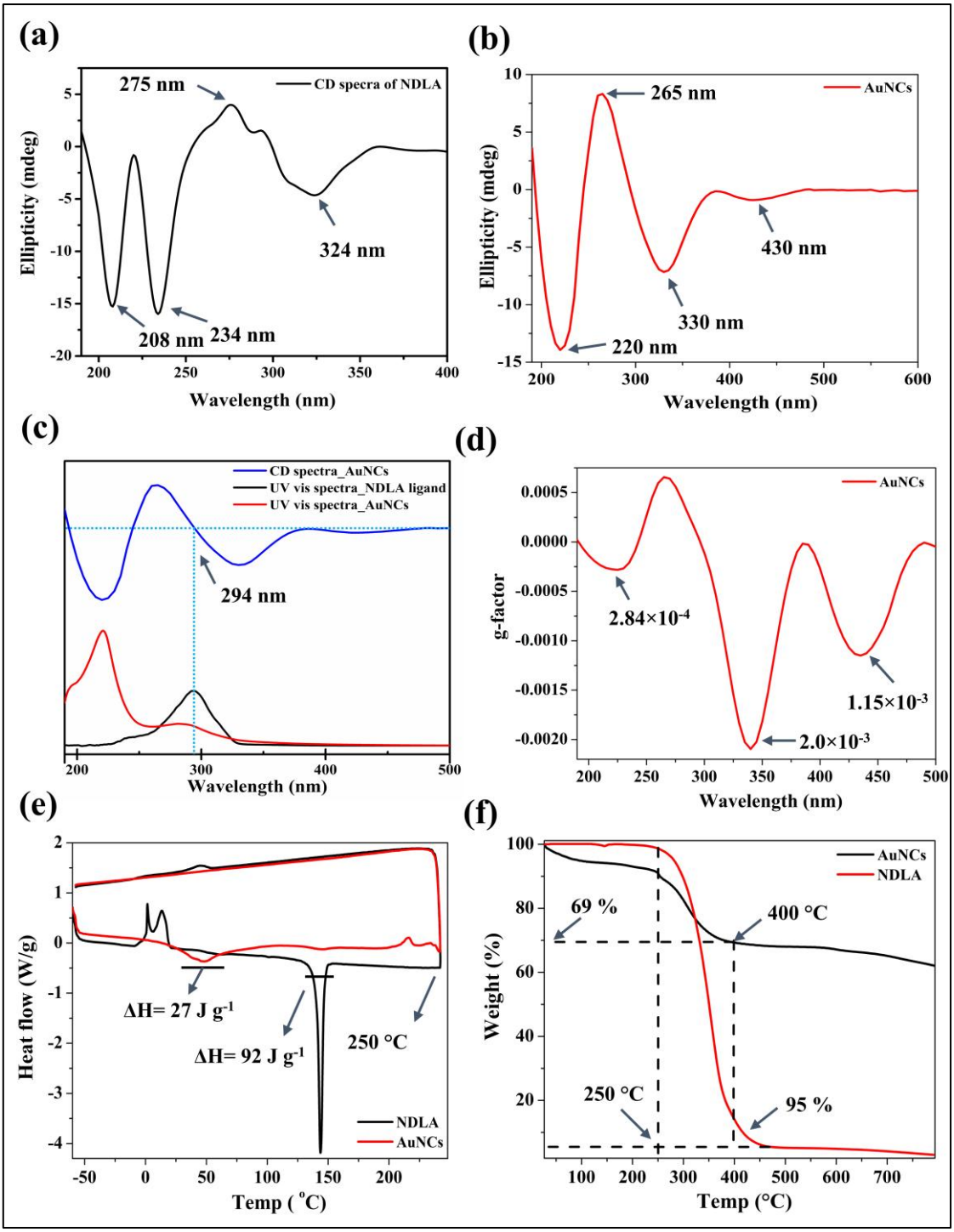


Figure 3. (a) Circular dichroism (CD) spectra of NDLA ligand; (b) Circular dichroism (CD) spectra of NDLA-AuNCs; (c) CD and UV-vis spectra of NDLA-AuNCs showing excitonic coupling, with the absorption band located near the zero crossing of the CD signal; (d) Anisotropy factor analysis of AuNCs; (e) DSC profiles of NDLA ligand and corresponding NDLA-AuNCs; (f) TGA profiles of NDLA ligand and the NDLA-AuNCs.

The quantitative evaluation of the induced optical activity was further evaluated by calculating the wavelength-dependent anisotropy factor, g(λ), over the relevant spectral region using the following eq. 1,

$$g(\lambda) = \theta(\lambda) / (32{,}980 \times A(\lambda)) \quad (1)$$

where θ (λ) is the ellipticity in millidegrees (mdeg) and A (λ) is the corresponding absorption. The g-factor spectrum shows alternating positive and negative Cotton effects with a positive maximum at 270 nm (5×10^{-4}) and a negative minimum at 340 nm (2×10^{-3}), consistent with the previously reported values on atomically precise AuNCs **[Figure 3(d)]**.[64] The pronounced negative peak near 340 nm indicated a strong chiral response associated with electronic states that bridge ligand-derived orbitals and the delocalized Au core states. Here, the wavelength dependence of the g-factor highlights a complex interplay of electronic coupling within the cluster, which is attributed to direct interaction of the chiral ligands with the gold core at the interface, further re-enforcing the ligand-induced chirality phenomenon.[65]

Differential scanning colorimetry (DSC) and thermogravimetric analysis (TGA) were carried out to probe the thermal stability and ligand environment of the NDLA-AuNCs in comparison with the free ligand. The DSC thermogram of the ligand displayed a sharp endothermic melting peak with an onset at 141 °C and a maximum at 144 °C **[Figure 3(e)]**. The small peak width and the large enthalpy change (ΔH ≈ 92 J g^{-1}) exhibited that the material is highly crystalline in its bulk form. This crystallinity likely arises from the π–π interactions and van der Waals forces between the aromatic groups and aliphatic units. The sharp decomposition peak observed at around 250 °C is attributed to the degradation of the ligand and cleavage of the bonds within its organic backbone. In contrast, the thermogram of AuNCs exhibited a different thermal profile. The broad endothermic peak extending from 30 °C to 48 °C (ΔH ≈ 27 J g^{-1}) is attributed to the desorption of weakly bound solvents or moisture. Interestingly, the absence of the prominent sharp endotherm of the free ligand indicated complete loss of long-range crystalline order upon coordination with the gold core. This is probably due to the chiral nature of the ligand, which hinders the ordered packing on the curved gold surface and adopts a conformationally disordered arrangement. A minor endothermic transition is also observed between 211 °C and 216 °C (ΔH ≈ 4.4 J g^{-1}), which can be assigned to the onset of the ligand decomposition or structural reorganization of the gold surface.

Further, the complementary insights from the TGA showed a sharp weight loss of the NDLA ligand starting around ~250 °C, which almost completely decomposed at ~400 °C **[Figure 3(f)]**. In contrast, the NDLA-AuNCs exhibited weight loss below 150 °C, corresponding to the desorption of the solvent or moisture residues, followed by a broader decomposition between 250–400 °C associated with the breakdown of strongly bound di-thiolate ligands. Beyond 400

°C, the AuNCs retained ~69 % weight, which can be attributed to the thermally robust metallic Au core. Taken together, the DSC and TGA analyses establish the fact that the ligand anchoring onto the AuNCs core not only disrupts the crystalline order but also confers superior thermal stability by strengthening interfacial bonding.

Following the comprehensive physicochemical analysis of the NDLA-AuNCs system, the charge transfer behaviour and the underlying transport mechanism were investigated to determine the efficiency of the charge carriers propagating through the nanoclusters network. Such an insight is critical for rational optimization of material, as even structurally well-defined nanomaterials may exhibit suboptimal functionality if charge transfer remains restricted or inefficient. Keeping this in mind, the temperature-dependent electrical conductivity of AuNCs was measured in the range of 100–300 K. An incrementation of direct current (DC) conductivity with temperature was observed, which pointed towards the semiconducting behaviour as electrical conductivity of 4.18 x 10^{-8} S/m was noted at 300 K for the NDLA based nanoclusters system **[Figure 4(a)]**.

To gain a deeper insight into the charge transport mechanism, the data was analyzed using the Arrhenius equation (eq. 2),

$$\sigma(T) = \sigma(0)\, exp\left[-\frac{Ea}{k_B \times T}\right] \quad (2)$$

where E_a is the activation energy, k_B is the Boltzmann constant, and T is the absolute temperature. The analysis of the Arrhenius plot ($\ln \sigma$ vs. 1/T) revealed two distinct linear regions corresponding to different temperature ranges **[Figure 4(b)]**. In the lower temperature range (100- 200 K), a low activation energy of 0.03 eV was observed, suggesting that the charge transport in this region is likely governed by thermally activated hopping conduction. Conversely, at an augmented temperature range (200-300 K), a comparatively higher activation energy of 0.23 eV is observed, suggesting the presence of thermally activated semiconducting behaviour. This dual-conducting behaviour holds significant implications for the next-generation functional nanomaterials, particularly in room-temperature gas sensing, thermoelectric energy conversion and low-power neuromorphic devices, where precise control over thermally activated and hopping-mediated conduction mechanisms is important for achieving optimal device performance.[66,67]

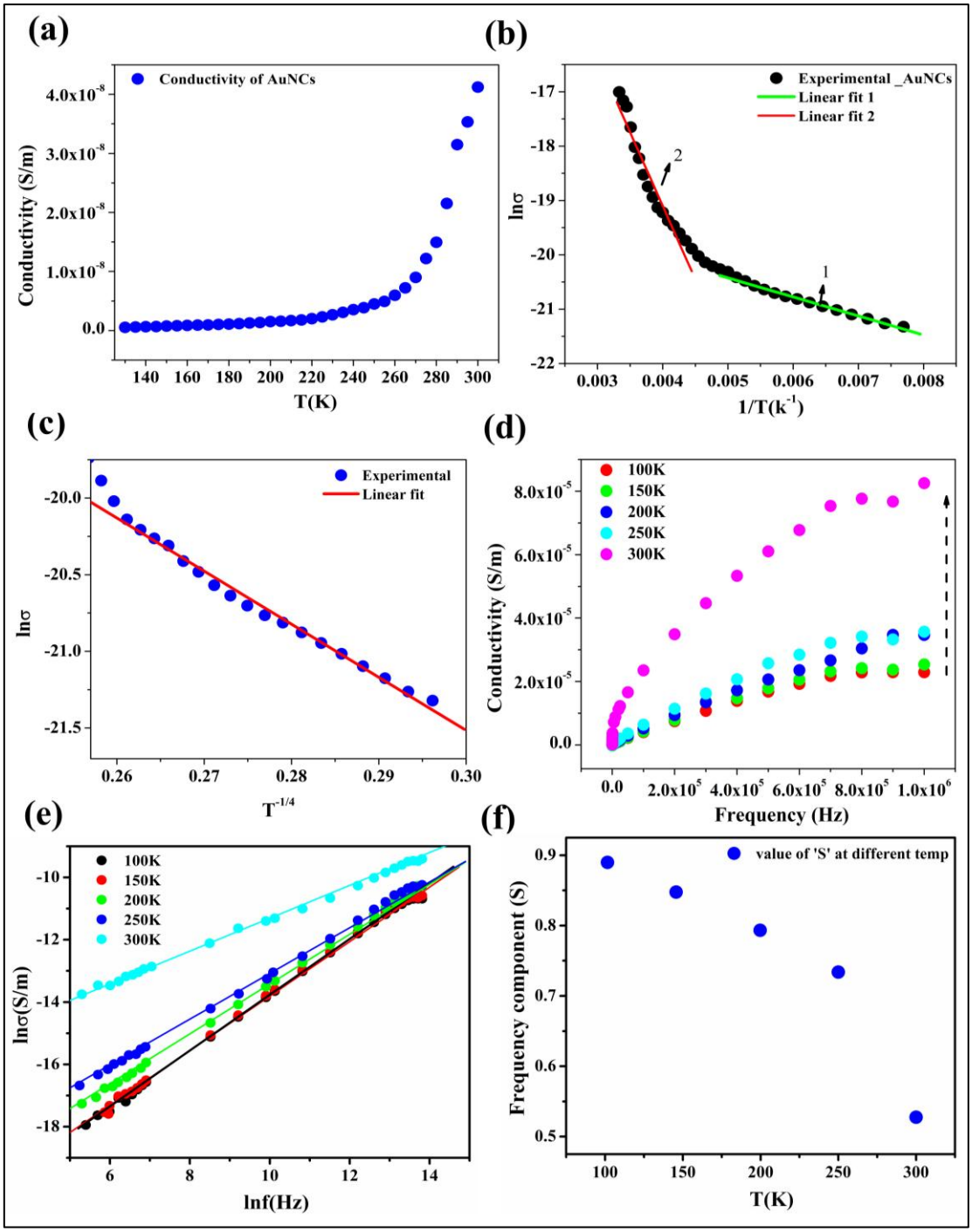


Figure 4 (a) Temperature-dependent conductivity of NDLA-AuNCs illustrating semiconducting behaviour; (b) Analysis of conductivity data using the Arrhenius model reveals two distinct activation energies; (c) Conductivity data of the NDLA-AuNCs fitted to the Mott 3D VRH model ($\ln\sigma$ vs $T^{-1/4}$); (d) Frequency-dependent conductivity showing a temperature-dependent increasing pattern; (e) linear variation of ln [$\sigma_{ac}(f)$] with ln (f) at temperatures of 100-300K; (f) the correlated barrier hopping (CBH) model indicates the decrease of 's', with increasing temperature.

For the investigation of the mechanistic aspect of low-temperature conduction, the data was analyzed using Mott's variable-range hopping (VRH) theory.[68,69] According to this theory, the conductivity was calculated using eq. 3 and 4,

$$\sigma(T) = \sigma_0 (\frac{T_{Mott}}{T})^{\frac{1}{2}} exp[-\left(\frac{T_{Mott}}{T}\right)^{\gamma}] \quad (3)$$

$$T_{Mott} = \frac{16}{k_B N(E_F) L_{loc}^3} \quad (4)$$

where the exponent γ specifies the effective dimensionality of the charge-transport network. The corresponding values of γ were taken as 1/4, 1/3 , and for three-dimensional, two-dimensional, and one-dimensional systems, respectively. The σ_o denotes the conductivity in the limit of infinite temperature, T_{Mott} is the characteristic Mott temperature, k_B represents the Boltzmann constant, $N(E_F)$ is the density of electronic states at the Fermi level, and L_{loc} is the localization length. The charge-transport mechanism and the electrical conduction behaviour of the AuNCs was analyzed using the ln σ(T) vs $T^{-1/4}$ plot [**Figure 4(c)]**. The observed linear variation in the plot indicated that these nanoclusters follow a three-dimensional (3D) charge transport (for γ =1/4) mechanism with a corresponding T_{Mott} value of 1.4×10^6 K.

The exploration of the dc conductivity under the influence of magnetic field strength (1T) demonstrated a decrease in magnetoconductivity with increasing temperature from 100 K to 300 K. This behaviour can be explained by the wave function shrinkage model.[70,71] According to this model, the wave functions of electrons contract under the influence of a magnetic field and reduce the average hopping length, which leads to negative magnetoconductivity **[Figure S13]**. For a small magnetic field, the magnetoconductivity ratio can be expressed by eq. 5,

$$ln\left(\frac{\sigma(B,T)}{\sigma(0,T)}\right) = -t_1 \frac{e^2 L_{loc}^4}{\hbar^2} \left(\frac{T_{Mott}}{T}\right)^{\frac{3}{4}} B^2 \quad (5)$$

where the numerical constant of order unity (t_1) = 5/2016, B is the magnetic field, T_{Mott} is the characteristic Mott temperature, and L_{loc} is the localization length. [71] The experimental data was fitted in equation 5, and the values of L_{loc} and density of states (DOS) at the Fermi level [$N(E_F)$] were calculated to be 0.3 nm and 4.9×10^{21} states· eV^{-1}· cm^{-3}.

The alternative current (AC) conductivity of the AuNCs was evaluated by measuring the capacitance (Cp) and dissipation factor (D) as a function of frequency, over the same temperature range (100-300 K) **[Figure 4(d)]**. In many amorphous semiconductors or disordered materials, the electrical conductivity typically includes a dc-contribution (σ_{dc}), along with the ac-conductivity (σ_{ac}). Thus, over a broad frequency range at a fixed temperature, the overall conductivity generally follows the pattern, known as universal dielectric response, which is described in the eq. 6,

$$\sigma'(f) = \sigma_{dc} + \sigma_{ac}(f) = \sigma_{dc} + \alpha f^{s} \quad (6)$$

where α is a temperature-dependent constant, f is the measuring frequency, and 's' is the frequency exponent.[72] The resultant data demonstrated that the variation of conductivity at higher frequencies was due to the dc-contribution. In addition, the frequency-dependent part, $\sigma_{ac}(f)$, can be calculated by subtracting the dc-contribution from the total conductivity. The linear variation of ln [$\sigma_{ac}(f)$] with ln (f) at different temperatures revealed that the slope of the plot decreases as the temperature increases. **[Figure 4(e)]**.

In general, the charge transport mechanism for the discrete systems is governed by two physical processes, one being correlated barrier hopping (CBH) and the other being quantum mechanical tunnelling.[73,74] The decrease in the frequency component (s) with increasing temperature as observed in the NDLA-AuNCs suggested that the charge conduction process is governed by the CBH model **[Figure 4(f)]**. Collectively, the temperature-dependent electrical conductivity measurements revealed that the π-conjugated ligand (NDLA) stabilized AuNCs assembly follow the Mott VRH transport model in the temperature range of 100-300 K. The calculated localization length of 0.3 nm indicated that the inter-cluster electronic coupling is weak and the charge transport occurs predominantly through phonon-assisted hopping between spatially localized states rather than through extended metallic conduction pathways. These results represent an important class of granular metallic nanostructures in which electron transport is governed by inter-cluster hopping and disorder-induced localization rather than extended band conduction. The tunable transport behaviour through cluster size and ligand chemistry makes this material as an ideal candidate for exploration of quantum-confined charge transport and for the developing chemically tailorable nanoscale electronic materials.

The key charge transport parameters, such as activation energies, localization length and the hopping conduction behaviour, are strongly influenced by the distribution of the oxidation states and surface redox chemistry within the lattice of the nanomaterials. Therefore, it becomes essential to investigate the redox behaviour of the synthesized AuNCs. For this purpose, cyclic voltammetry (CV) analysis was performed in 0.1 (M) TBAF/acetonitrile electrolyte, using an $Ag/AgNO_3$ reference electrode **[Figure S14]**. The resultant voltammogram displayed a well-defined redox pair, characterized by distinct anodic and cathodic peaks at -0.33 V and -0.63 V, respectively. The anodic peak exhibited a current (Ia) of + 5 μA, while the cathodic peak showed a current (Ic) of -10 μA. The electrochemical band gap of the NDLA-AuNCs was also determined to be 0.8 eV, with corresponding HOMO and LUMO energy levels of 5.042 eV and 4.242 eV, respectively. The presence of distinct anodic and cathodic peaks indicates that

the AuNCs undergo redox processes rather than exhibiting featureless metallic behaviour, thereby confirming their redox activity with well-defined electron-transfer capabilities. The electrochemically accessible surface area was further evaluated using CV analysis in the non-faradic region at different scan rates (20 to 140 mVs^{-1}) **[Figure 5(a)]**. The gradual increase of symmetric anodic and cathodic current density with increasing scan rate supported the capacitive nature with a high electroactive surface area of the NDLA-AuNCs. To quantify the double-layer capacitance (C_{dl}), capacitive current densities at a fixed potential were plotted as a function of scan rate, which disclosed a linear dependence on scan rate. From the slope of this plot, double-layer capacitance (C_{dl}) was determined to be 11.21 mF/ cm^2 **[Figure 5(b)]**. This C_{dl} value is notably higher than any previously reported values for pristine, unmodified gold nanoclusters, which have been typically between 0.001-0.120 mF/ cm^2, suggesting that the higher capacitance arises from both the nanocluster core and surface ligand induction.[75,76] The relatively high C_{dl} value reflects a large electrochemically active surface area (ECSA) of 280.2 cm^2, which is beneficial for surface-controlled electrochemical applications, including electrocatalysis, supercapacitors, sensors, and photoelectrochemical systems, where the interfacial charge storage and surface accessibility play a crucial role in performance.

This extraordinary combination of prominent redox activity and electrical conductivity makes these NDLA-AuNCs extremely useful for electrocatalytic applications, where the large active surface area allows facile electron transfer during reactions. Additionally, in biological systems, AuNCs can also presumably interact with the nearby biomolecules by exchanging electrons, which can help to control the ROS levels inside the cells. Due to this electron exchange ability, the AuNCs seems to possessthe potential for exhibiting biological activity, including ROS-mediated therapeutic applications, as discussed in latter sections.

The influence of the electrical conductivity and redox-active surface area of the AuNCs on their catalytic activity and charge-transfer property was further evaluated by considering the hydrogen evolution reaction (HER) as a model electrocatalytic process. For this purpose, the electrochemical hydrogen evolution reaction (HER) activity of the NDLA-AuNCs was systematically investigated in alkaline media by performing cyclic voltammetry (CV), linear sweep voltammetry (LSV), and chronoamperometry measurements, with all potentials referenced to the reversible hydrogen electrode (RHE). It was observed that these electrochemical measurements exhibited minimal hysteresis, indicating rapid interfacial charge transfer and a reversible electrochemical process in 1 (M) KOH electrolyte **[Figure S15]**.

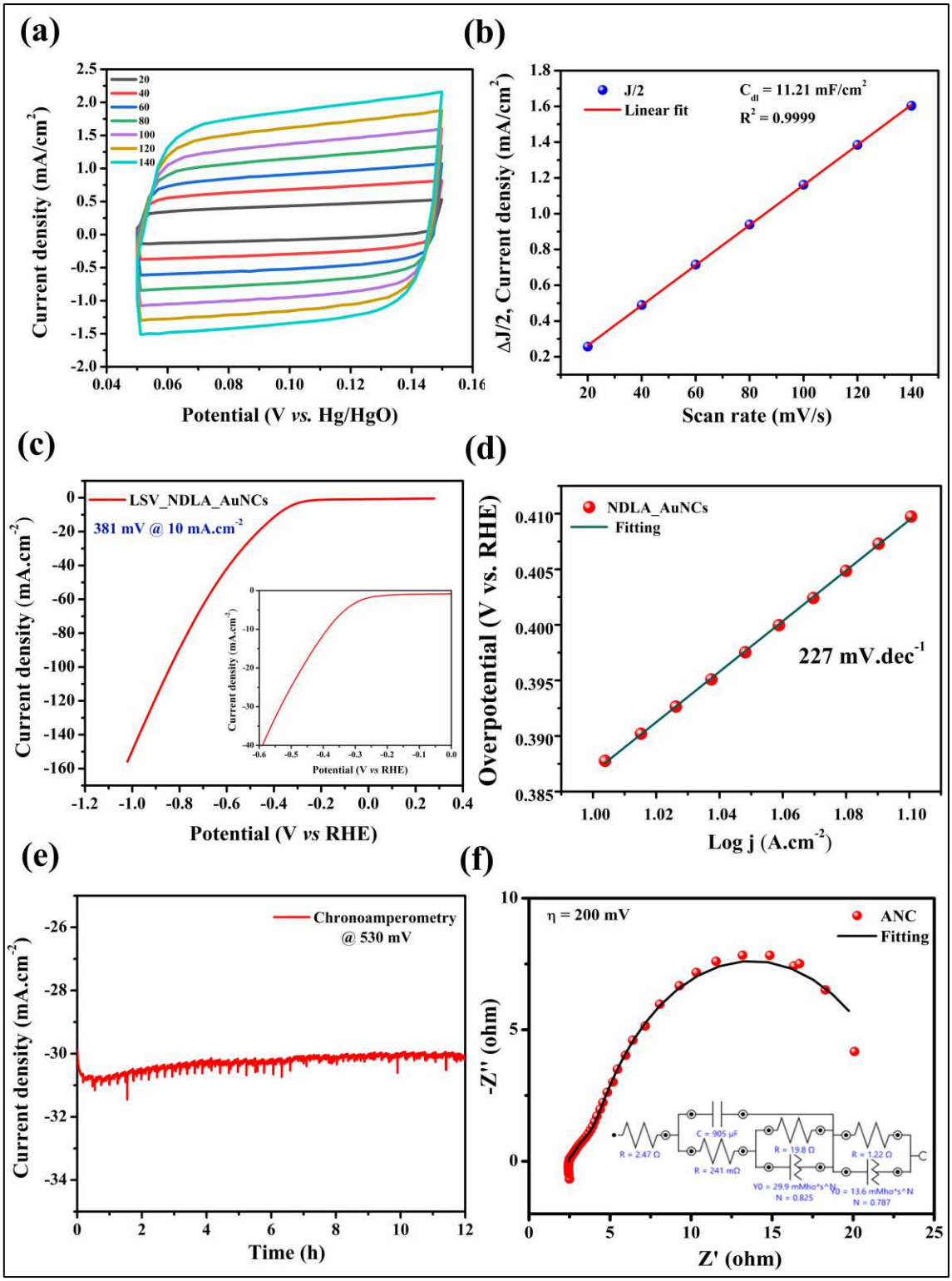


Figure 5. (a) CV-analysis of NDLA-AuNCs in the non-faradic region was carried out at scan rates ranging from 20 to 140 mVs^{-1}; (b) Linear fitting of the capacitive currents versus CV scan rates for NDLA-AuNCs to calculate the electrical double-layer capacitance; (c) Linear sweep voltammetry (LSV) curve toward HER in 1 (M) KOH; (d) Corresponding Tafel plot of NDLA-AuNCs; (e) Long-term stability test of NDLA-AuNCs for the HER at an overpotential (η) of 530 mV; (f) Nyquist plot and equivalent circuit model for the analysis of EIS data of studies electrode in 1 (M) KOH solution.

The LSV measurement displayed a well-defined HER polarization curve, with a current density of 10 mA cm^{-2} at an overpotential of 381 mV [**Figure 5(c)]**. It is pertinent to note here that although the use of AuNCs as an electrocatalyst for the HER is well established, the existing reports display relatively high overpotentials, typically exceeding 500 mV to achieve a current density of 10 mA cm^{-2}. In contrast, the present experimentation involving NDLA-AuNCs demonstrated significantly improved performance by achieving both lower overpotential (381 mV at 10 mA cm^{-2}) and higher current densities, exceeding the performance of any reported bare AuNCs systems so far **[Table S2]**. The obtained Tafel slope value of 227 $mVdec^{-1}$ suggests that the Volmer process is the rate-determining step (RDS), and the HER mechanism proceeds through the Volmer-Heyrovsky pathway **[Figure 5(d)]**. The long-term chronoamperometry conducted at a higher potential of 530 mV revealed the robust performance over a 12-hour duration **[Figure 5(e)]**. The relative current density also indicated strong stability, with the initial current density largely retained after 12 hours **[Figure S16]**. The absence of abrupt current decay confirmed the long-time durability of the NDLA-AuNCs against agglomeration and dissolution in alkaline media.

Additionally, electrochemical impedance spectroscopy (EIS) was performed to investigate the charge transfer resistance (R_{ct}) of the electrocatalysts during the HER process. AuNCs exhibited a very low R_{ct} value of 21 ohms, which indicated the fast charge transfer on the interface of the catalyst surface and electrolyte during the HER process **[Figure 5(f)]**. Overall, these results highlighted that the high electroactive surface area of the nanoclusters system and the presence of π-conjugated ligand shell facilitate rapid electron transfer across the ligand-metal interface, thereby significantly reducing the R_{ct} value at the electrode-electrolyte region. Moreover, the kinetically sluggish alkaline electrolytes are less corrosive and economically viable, which makes them promising for industrial-grade hydrogen production through water electrolysis. Such transformation of the inactive gold metal into a dynamically adaptive and stable HER electrocatalyst provides a promising platform for the rational design of noble-metal-based electrocatalysts.

The pronounced redox activity and facile electron transfer properties of these nanoclusters, facilitate controlled electron exchange with the surrounding dissolved oxygen, leading to the formation of highly reactive species such as superoxide and hydroxyl radicals. Therefore, the ROS generation capability of the NDLA-AuNCs was systematically evaluated using both normal (NIH-3T3 fibroblasts & C2C12 myoblasts) and cancer cell (4T1 triple negative breast cancer) models, along with the elucidation of the associated mechanistic pathways. To this end, the concentration-dependent cell viability was first determined with different concentrations

(0.05–0.4 mg·mL^{-1}) of the NDLA-AuNCs, using a colorimetric MTT assay. The results demonstrated that the NDLA-AuNCs caused negligible cytotoxicity towards normal NIH-3T3 and C2C12 cells at concentrations up to 0.1 mg·mL^{-1} **[Figure 6(a)]**.

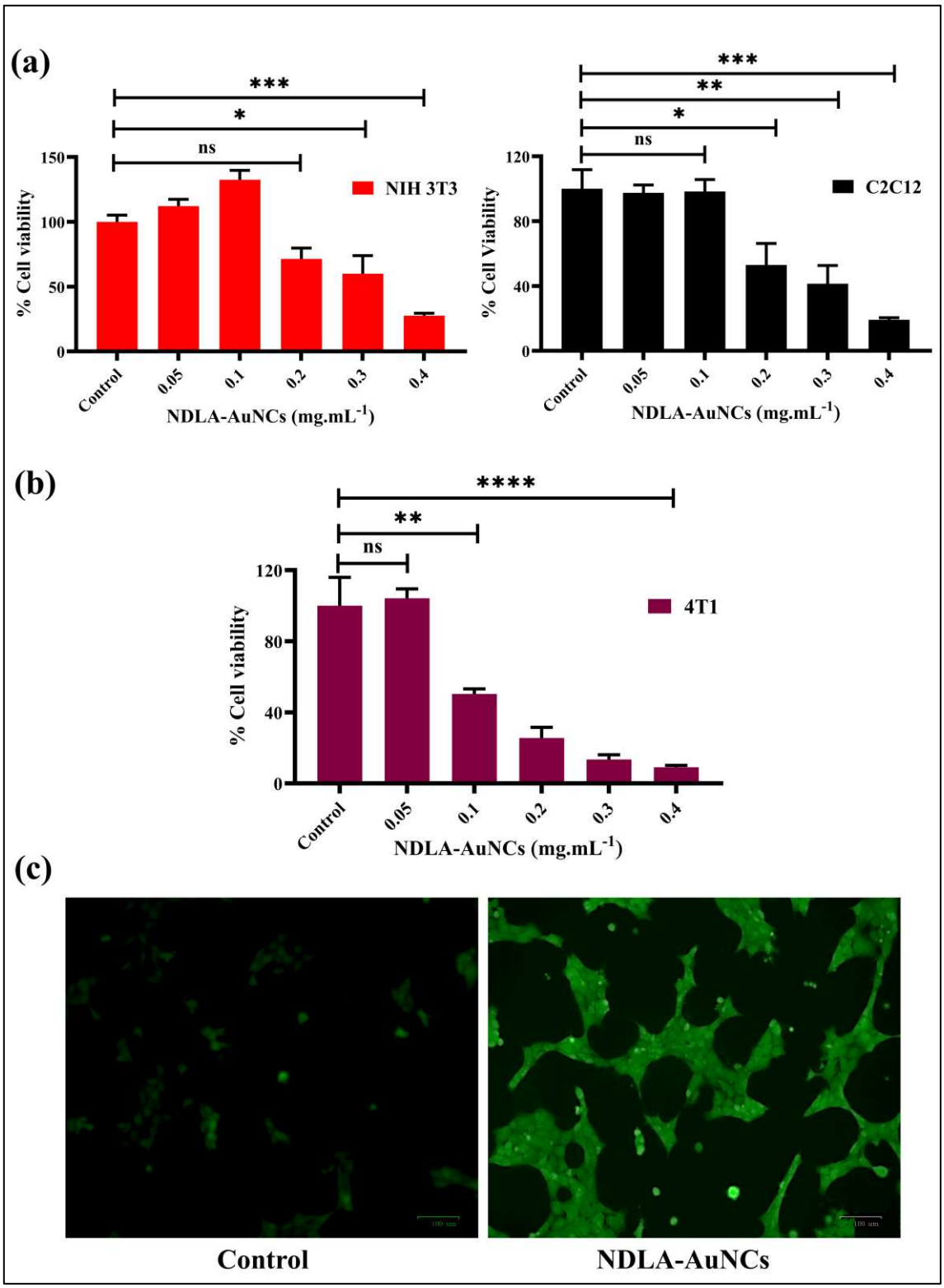


Figure 6. (a) *In vitro* cytotoxicity analysis of NDLA-AuNCs using NIH 3T3 and C2C12 cells; (b) Cytotoxicity analysis towards 4T1 cancerous cells; (c) Microscopic image of intracellular ROS

generation in NDLA-AuNCs treated 4T1 cells using DCFH-DA dye (0.1 mg·mL^{-1} dose; scale bar 100 µm). *p<0.01; **P< 0.001; ***P< 0.0001; ****P< 0.00001 versus control.

However, when the concentration exceeded this level, cell viability gradually decreased in a dose-dependent manner. In contrast, the cancerous 4T1 cells exhibited a significant reduction in viability even at 0.1 mg·mL^{-1} **[Figure 6(b)]**. These observations suggest that 0.1 mg·mL^{-1} is a safe concentration for normal cells while still exhibiting substantial anticancer activity. The mitochondrial membrane potential (MMP) was then analyzed to understand the mechanism of cell cytotoxicity induced by AuNCs. In healthy, metabolically active cells, JC-1 dye accumulates in polarized mitochondria and forms aggregates that emit red fluorescence **[Figure 7]**.

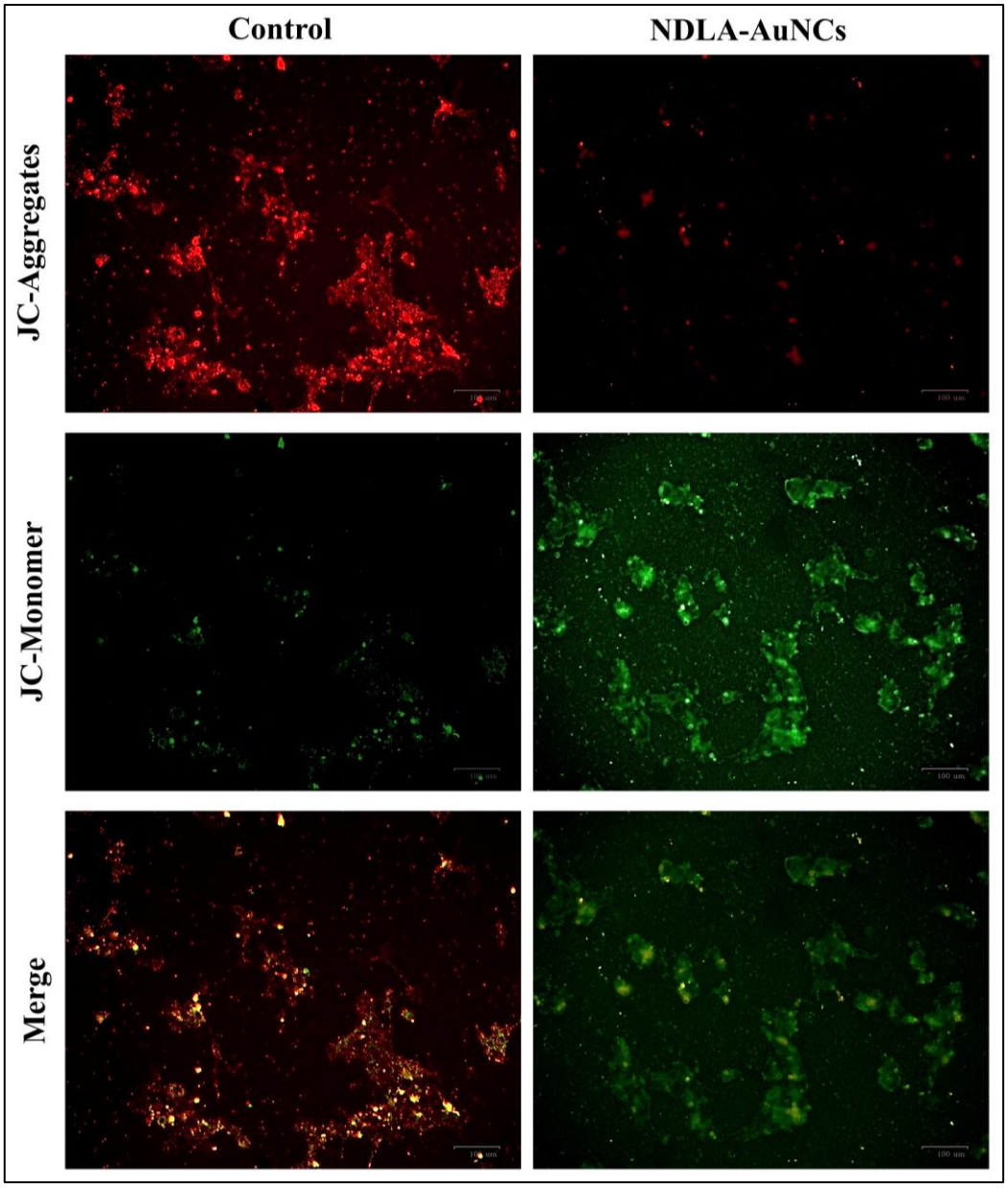


Figure 7. Analysis of mitochondrial membrane potential disruption in 4T1 cells upon treatment of NDLA-AuNCs, using JC-1 assay.

When mitochondria lose their membrane potential, JC-1 remains as monomers in the cytosol and emits green fluorescence. However, the NDLA-AuNCs treated 4T1 cells at 0.1 $mg \cdot mL^{-1}$ displayed a significant reduction in the red-to-green fluorescence intensity ratio, which indicated mitochondrial depolarization and the initiation of programmed cell death **[Figure S17 (a)]**. The involvement of ROS in this mitochondrial damage was further checked using the 2,7-dichlorofluorescein diacetate (DCFH-DA) assay as a fluorescent indicator **[Figure 6(c)]**. The relative fluorescence quantification and microscopic analysis demonstrated that the ROS levels in the treated 4T1 cells were significantly increased **[Figure S17(b)]**. This indicates that

oxidative stress plays a major role in the cell damage caused by the treatment of the NDLA-AuNCs.

Following the confirmation of *in vitro* ROS-mediated anticancer activity, the photodynamic activity of AuNCs was also investigated using 690 nm NIR laser irradiation. When the NDLA-AuNCs-treated 4T1 cells were exposed to the laser, a significant amount of ROS was produced, compared to the non-irradiated control **[Figure S18]**. Additionally, the quantitative fluorescence intensity analysis confirmed this observation and demonstrated that the NDLA-AuNCs also possess effective photodynamic property **[Figure S17 (c)]**.

Building upon the observed *in vitro* anticancer property and NIR-induced photodynamic activity, it was further necessary to determine whether these results also translate into therapeutic effectiveness and safety under physiological conditions. Therefore, a detailed *in vivo* toxicity study of the NDLA-AuNCs was performed using the BALB/c mice model **[Figure 8(a)]**. After fourteen days of continuous treatment, the animals were sacrificed, and a detailed analysis of blood biochemistry, liver functions, and histological assay of the major organs were performed. The blood parameters showed that the hemoglobin levels remained unchanged, which demonstrated that the continuous exposure to AuNCs did not affect the ability to carry oxygen or induce anemia in the blood **[Figure 8b (i-ii)]**. The preserved cell counts, intact shape and volume of the blood cells confirmed the absence of hematotoxic effects of the NDLA-AuNCs system **[Figure 8b(iii-vi)]**.

Similarly, total white blood cells, including neutrophils and lymphocytes, showed no significant changes. These results suggest that the NDLA-AuNCs are non-toxic and non-immunogenic in nature **[Figure 8b(vii-ix)]**. The hepatotoxicity of the treated animals was also evaluated by measuring the levels of important liver enzymes, such as alanine aminotransferase (ALT/ SGPT), alkaline phosphatase (ALP), and serum total protein (including serum albumin and globulin) **[Figure 8b(x-xii)]**. The absence of elevated serum levels, which are the main indicator of liver injury, further demonstrated that the treatment of NDLA-AuNCs did not induce any hepatocellular damage.

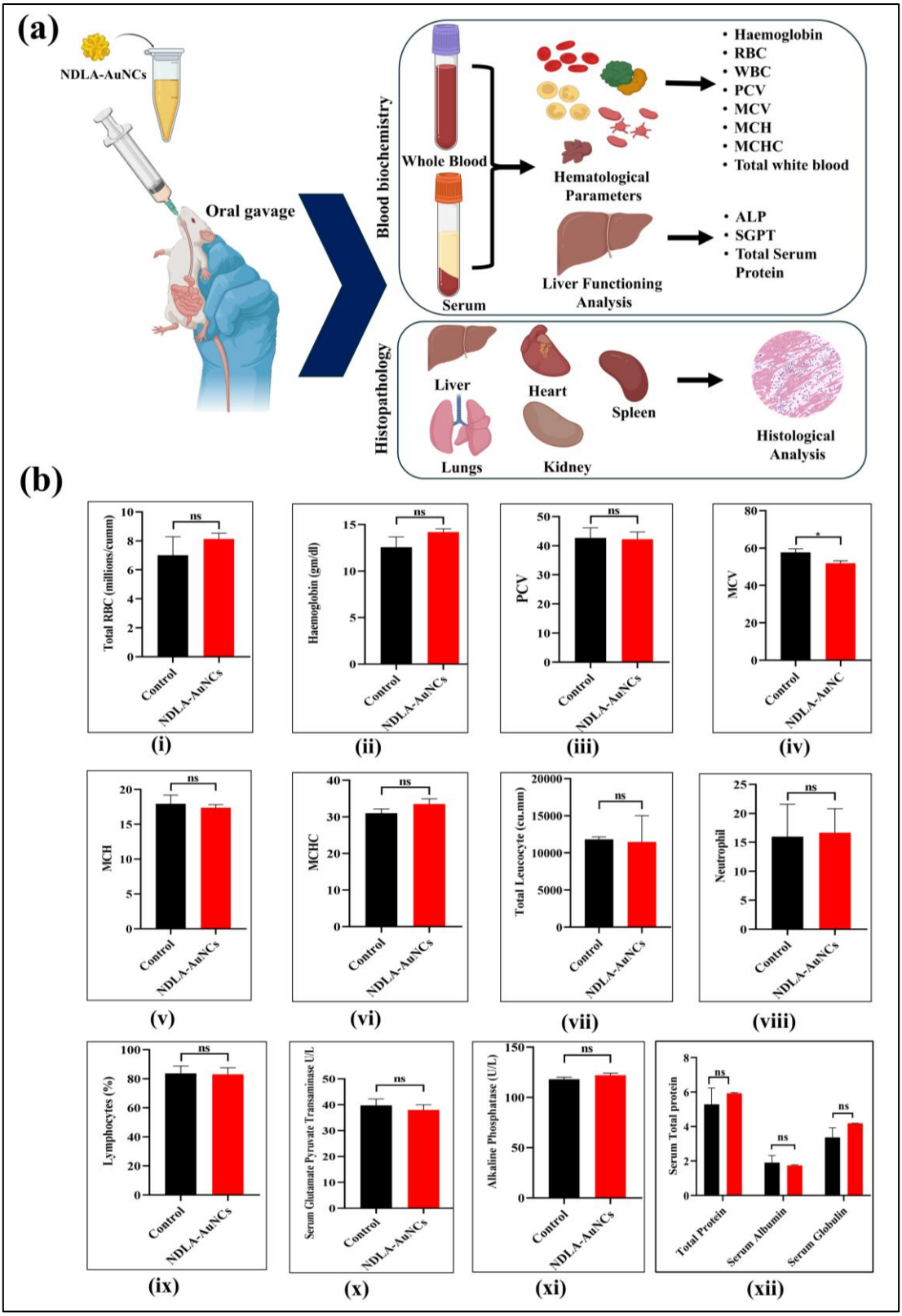


Figure 8. (a) Schematic representation of the experimental procedure for *in vivo* cytotoxicity assessment of NDLA-AuNCs using BALB/c mice model; (b)Haematological and blood biochemistry analysis of NDLA-AuNCs, including (i) erythrocyte count (million/cu.mm); (ii) hemoglobin (g/dL); (iii) packed cell volume (PCV); (iv) mean corpuscular volume (MCV); (v) mean corpuscular hemoglobin (MCH); (vi) mean corpuscular hemoglobin concentration (MCHC); (vii) total leukocyte count (per cu.mm); (viii) neutrophils count; (ix) lymphocytes count; (x) serum glutamate-pyruvate

transaminase (U/L); (xi) alkaline phosphatase (U/L); (xii) serum total protein, including serum albumin and serum globulin.

The histological evaluation of the major organs, such as liver, spleen, kidney, heart, and lungs of the treated animals revealed the preserved tissue structures and no significant differences between the NDLA-AuNCs treated and control groups **[Figure 9]**.

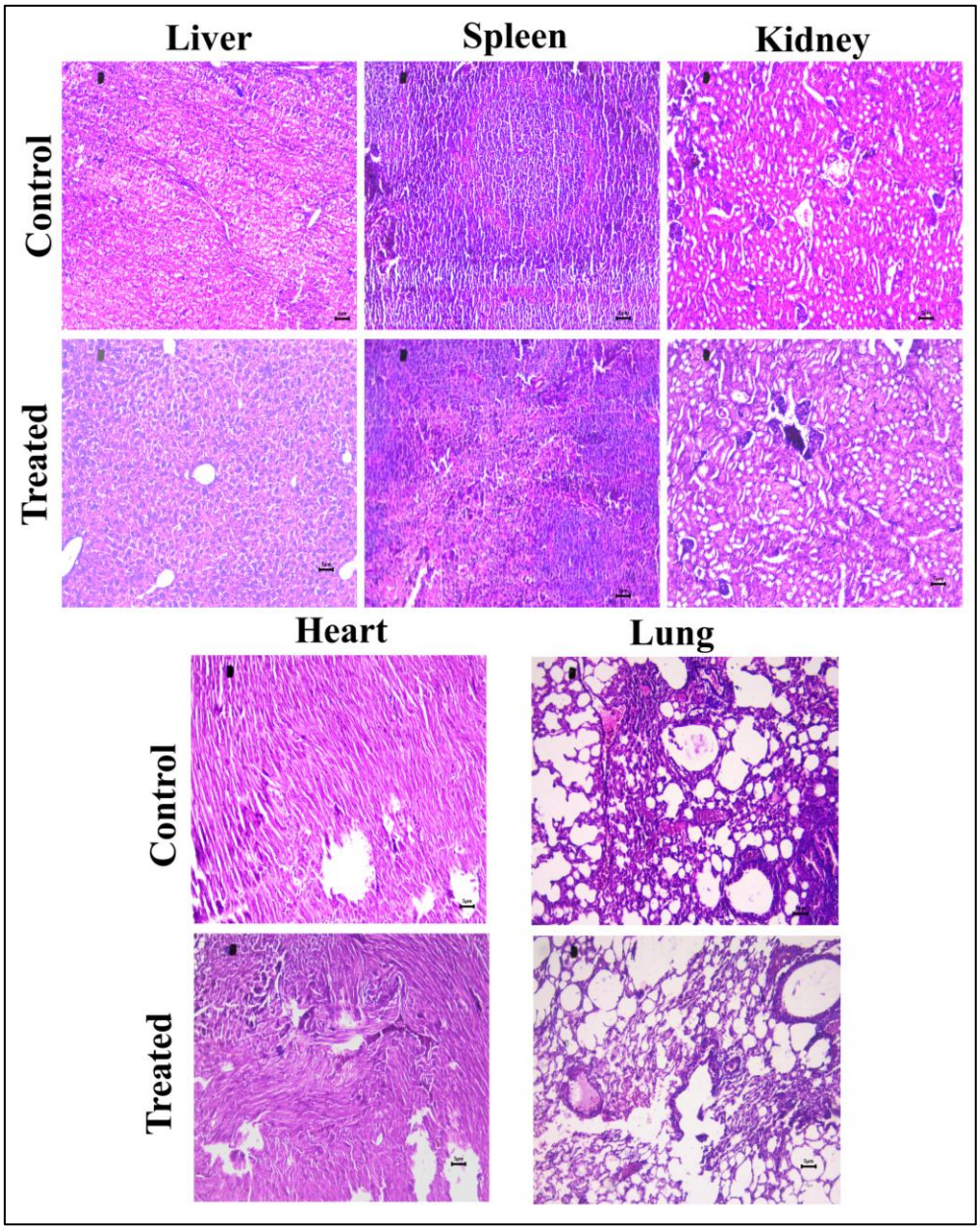


Figure 9. *In vivo* histopathology analysis of major organs: liver, spleen, kidney, heart, and lung using H & E staining upon treatment with NDLA-AuNCs (scale 5 µm).

The splenic tissue structure maintained its normal structure, and no signs of tissue loss or bleeding. Similarly, the histology analysis of the kidney was demonstrated to be normal

glomeruli and tubules, with no sign of scarring or damage. The heart tissue also appeared normal as well, with properly arranged muscle fibers. Collectively, these results suggest that the treatment of NDLA-AuNCs did not induce any noticeable blood toxicity, liver toxicity, as well as organ toxicity, and support a favorable biocompatible and non-immunogenic safety profile under the tested conditions.

3 Conclusion

In summary, this study demonstrated that the ligand engineering provides am effective strategy for programming the electronic structure and redox properties of ultrasmall AuNCs. Beyond serving as a stabilizing shell, the newly synthesized chiral NDLA ligand actively modulates the metal-ligand interface, leading to ligand induced exciton coupling, electrical semi-conductivity, redox activity, and efficient interfacial charge transport properties. The resulting NIR-active NDLA-AuNCs demonstrated a characteristic bi-signate Cotton effect that originates from exciton-coupling between the adjacent clusters. The extended chiral signal beyond the ultraviolet region suggests that the molecular chirality of the ligand effectively transferred to the electronic structure of the AuNCs core. The influence of this structural-electronic coupling is also reflected in the electron transfer properties of the AuNCs system.

The temperature-dependent conductivity measurements revealed semiconducting behaviour, where the electron transport at low temperature occurs through a 3D-VRH hopping mechanism. The overall conduction process follows the correlated barrier hopping model, suggesting that the electrons are moved between localized states with the help of thermal energy. The calculated localization length of 0.3 nm indicates that the charge carriers are strongly localized across the nanoclusters network. The CV measurements display clear anodic and cathodic peaks, demonstrating that the NDLA-AuNCs possess intrinsic redox activity. In addition, the non-faradic CV measurements reveal a higher double-layer capacitance value of 11.21 mF/cm^2 and a large ECSA of 280.2 cm^2. Together, these properties help to facilitate efficient charge transfer kinetics, abundant active sites, and structural stability, which improves the electrocatalytic performance of the NDLA-AuNCs system for the hydrogen evolution reaction. Interestingly, the same electronic properties of this material also influence the biological activities. The *in vitro* cell cytotoxicity studies using normal as well as triple-negative breast cancer cell model revealed that the NDLA-AuNCs selectively kill highly aggressive and transplantable triple-negative breast cancer cells, while maintaining a favourable biosafety under physiological conditions. Additionally, the mechanistic analysis indicates that the anticancer activity arises from the intracellular ROS generation. The facile electron transfer of

the AuNCs promotes redox reactions that convert molecular oxygen into reactive species, which induce mitochondrial damage and eventually cause cancer cell death. Consistent with this mechanism, the photodynamic activity of this NDLA-AuNCs system was evaluated. When the nanoclusters are exposed to 690 nm laser light, the ROS-production level increases significantly. This indicates that the photo-excitation enhances electron-transfer processes and subsequently the intracellular ROS-production is also increased.

Collectively, this study demonstrated that engineering the ligand shell is a powerful approach for transforming metal nanoclusters into multifunctional redox-active nanomaterials. By combining electrocatalytic hydrogen production and ROS-mediated biological activity in a single, biocompatible material platform, this work highlights a generalizable strategy for the development of multifunctional platform, capable of operating across the separated disciplinary boundaries through a common electron-transfer mechanism. In particular, the ability to couple molecular hydrogen generation with therapeutic intervention to treat acute lung injury, metabolic syndrome, parasite-induced liver inflammation, antimicrobial treatment, electrochemical sensing, and neurodegenerative diseases, as well as ROS-mediated biomedical treatment.

Overall, these findings provide a general design principle for coupling molecular chirality and ligand electronics to tailor nanocluster functionality towards integrated electrochemical-biomedical platforms and establish a foundation for future and most underexplored field of hybrid catalytic systems that are capable of simultaneous energy transformation and bioactive regulation towards translational applications.

4. Experimental Section

4.1 Materials

Gold (III) chloride trihydrate ($HAuCl_4.3H_2O$), potassium hydroxide (KOH, 99%), and 5% Nafion™ 117 solution were purchased from Sigma-Aldrich, alpha-naphthylamine, 1-hyroxybenzotriazole, and 4-dimethylaminopyridine were purchased from Hyma chemicals, , (R)-5-(1,2-dithiolan-3-yl)-pentanoic acid was purchased from BLD pharma, 1-(3-dimethylaminopropyl)-3-ethylcarbodiimide hydrochloride (EDC·HCl), triethylamine (TEA) were purchased from Sisco-Research Laboratory (SRL), ultrapure water (18.2 $M\Omega \cdot cm^{-1}$) was taken from Merck Millipore-Q3 system, the organic solvents were purchased from Merck.

4.2 Synthesis

4.2.1 Ligand Synthesis

In a dry round-bottom flask, (R)-5-(1,2-dithiolan-3-yl)-pentanoic acid (2.42 mmol, 500 mg) was dissolved in 10 ml of anhydrous DMF. The solution was cooled in an ice-bath under continuous stirring. Subsequently, 1-(3-dimethylaminopropyl)-3-ethylcarbodiimide hydrochloride (EDC·HCl) (3.15 mmol, 603 mg) and 1-hyroxybenzotriazole (HOBt) (2.66 mmol, 360 mg) were added to activate the carboxylic acid. After stirring for 10–15-minute, alpha-naphthylamine (2.66 mmol, 381 mg) and 4-dimethylaminopyridine (10 mg, cat. amount) was added, followed by triethylamine (0.74 ml, 5.2 mmol) to neutralize the HCl, and maintain the basic environment. The reaction mixture was stirring overnight under inert atmosphere. The progress of the reaction was monitored by thin-layer chromatography (TLC). Upon completion, the reaction mixture was poured slowly into ice-cold water to precipitate the product. The solid obtained was filtered and washed thoroughly with water. The crude product was dissolved in chloroform and washed three-times with water to remove all the water-soluble impurities and side-products. The organic phase was collected and evaporated the solvent under reduced pressure. Finally, the crude product was purified by column chromatography using 0.5 % methanol-chloroform mixture as the eluent and afford the pure product, (R)-5-(1,2-dithiolan-3-yl)-N-(naphthalen-1-yl)-pentanamide (NDLA), as solid **[Scheme 1(a)]**. (Yield = 70%, 560 mg)

^{1}H NMR (500 MHz, DMSO): δ 9.86 (s, 1H), 8.16 – 7.98 (m, 1H), 7.99 – 7.87 (m, 1H), 7.75 (d, *J* = 8.2 Hz, 1H), 7.67 (d, *J* = 7.4 Hz, 1H), 7.57 – 7.51 (m, 2H) , 7.48 (t, *J* = 7.8 Hz, 1H), 3.67 (p, *J* = 6.8 Hz, 1H), 3.21 (ddd, *J* = 11.0, 6.9, 5.5 Hz, 1H), 3.13 (dt, *J* = 11.0, 6.8 Hz, 1H), 2.49-2.39 (m, 3H), 1.90 (dq, *J* = 13.4, 6.8 Hz, 1H), 1.80 – 1.60 (m, 4H), 1.50 (q, *J* = 8.0 Hz, 2H) ppm.

^{13}C NMR (125 MHz, DMSO): δ 171.7, 133.7, 128.1, 125.9, 125.7, 125.5, 125.1, 122.7, 121.7, 56.2, 38.1, 35.7, 34.2, 28.4, 25.1.

ESI-MS: M+H= 332.12

4.2.2 Synthesis of NDLA-Gold Nanoclusters (NDLA-AuNCs)

In a typical synthesis, Gold (III) chloride trihydrate (HAuCl4.3H2O) (0.2 mmol, 79 mg) was dissolved in 0.79 ml of milli-Q (18.2 MΩ· cm) water, while the NDLA-ligand (0.3 mmol, 100 mg) was dissolved separately in 10 ml of isopropanol (IPA). A round-bottom flask equipped with a magnetic stir bar was charged with 15 ml of an IPA-water mixture (3:1 v/v) and placed on a magnetic stirrer. Under slow stirring, the aqueous gold precursor solution was added to the solvent mixture, followed by the dropwise addition of the ligand solution under vigorous

stirring. After 5 min of stirring, the pH of the reaction mixture was adjusted to 11 using 1 (N) NaOH solution. Subsequently, 0.5 ml of freshly prepared 10 mM $NaBH_4$ solution was added dropwise to the reaction mixture. The reaction flask was then immersed in an oil bath maintained at 40 °C and stirred for 12 h to complete the reduction and growth of the nanoclusters **[Scheme 1(b)]**.

To remove the excess ligand and unreacted impurities, the solvent was evaporated in reduced pressure then washed with chloroform then dried over the oven. The purified nanoclusters are then dispersed into the aqueous solution and followed by ultracentrifugation to improve the purity. Finally, the purified AuNCs solution was lyophilized to obtained the solid product and stored in 4 °C for further used. The images of synthesized nanoclusters in solid state and in liquid form along with TLC analysis using chloroform and methanol (3:2) as an eluent was shown in **[Figure S9]**.

Acknowledgments

This work was supported by funding from ANRF, New Delhi (CRG/2022/006638) granted to RKS. SKD is thankful to ANRF for providing research associateship. The authors are grateful to SAIF/ CIL and RUSA 2.0, Panjab University for providing access to sophisticated instrumental facilities. SM and KM acknowledged support from the ANRF, New Delhi (CRG/2022/003215) and the institutional instrumental facilities, Pandit Deendayal Energy University.

Authors contribution

SKD: Conceptualization, synthesis, and characterization of the materials; conducting research investigation processes; data acquisitions & formal analysis; original draft preparation; validation and visualization. SM, RB & KM: Investigation and analysis of electrochemical studies; data analysis; writing- review & editing; resources and validation. KG: Electrical conductivity study; writing and editing of manuscript; data analysis; validation. KI & AKR: Cell culture studies, ROS generation assay; review & editing; resources and validation. PC, SM & PC (IRH): In vivo cytotoxicity studies; data acquisitions & formal analysis; writing & editing. RKS: Supervision of overall research; writing- review & editing; project administration; funding acquisition; validation. The manuscript was written through contribution of all authors. All authors have given approval to the final version of the manuscript.

Conflict of Interest

The authors declare no competing financial interest

Data Availability Statement

The datasets used and/ or analyzed during the current study available from the corresponding author on reasonable request.

Reference

(1) Hughes, K. J.; Cheng, J.; Iyer, K. A.; Ralhan, K.; Ganesan, M.; Hsu, C.-W.; Zhan, Y.; Wang, X.; Zhu, B.; Gao, M. Unveiling Trends: Nanoscale Materials Shaping Emerging Biomedical Applications. ACS Publications 2024.

(2) Prajapati, D.; Jabborova, D.; Saharan, B. S.; Singh, N.; Patani, A.; Singh, S.; Joshi, C. Bionanotechnology: A Paradigm for Advancing Environmental Sustainability. *Indian J. Microbiol.* **2025**, *65* (1), 306–332.

(3) Zhang, F. Grand Challenges for Nanoscience and Nanotechnology in Energy and Health. *Frontiers in chemistry*. Frontiers Media SA 2017, p 80.

(4) Elzein, B. Nano Revolution:"Tiny Tech, Big Impact: How Nanotechnology Is Driving SDGs Progress. *Heliyon* **2024**, *10* (10).

(5) Maity, S.; Kolay, S.; Chakraborty, S.; Devi, A.; Patra, A. A Comprehensive Review of Atomically Precise Metal Nanoclusters with Emergent Photophysical Properties towards Diverse Applications. *Chem. Soc. Rev.* **2025**, *54* (4), 1785–1844.

(6) Kang, X.; Li, Y.; Zhu, M.; Jin, R. Atomically Precise Alloy Nanoclusters: Syntheses, Structures, and Properties. *Chem. Soc. Rev.* **2020**, *49* (17), 6443–6514.

(7) Du, X.; Jin, R. Atomic-Precision Engineering of Metal Nanoclusters. *Dalt. Trans.* **2020**, *49* (31), 10701–10707.

(8) Liu, Y.; Yu, J.; Lun, Y.; Wang, Y.; Wang, Y.; Song, S. Ligand Design in Atomically Precise Copper Nanoclusters and Their Application in Electrocatalytic Reactions. *Adv. Funct. Mater.* **2023**, *33* (44), 2304184.

(9) Pan, X.; Yao, Y.; Zhang, M.; Yuan, X.; Yao, Q.; Hu, W. Enzyme-Mimic Catalytic Activities and Biomedical Applications of Noble Metal Nanoclusters. *Nanoscale* **2024**, *16* (17), 8196–8215. https://doi.org/10.1039/D4NR00282B.

(10) Sun, Y.; Chen, Y.; Hu, X.; Liu, A.; He, L.; Dai, A.; Wei, T.; Wang, S.; Gan, Z. Multifunctional Gold Nanoclusters as Next-Generation Theranostic Platforms for Disease Management. *Int. J. Pharm. X* **2025**, *10*, 100361. https://doi.org/https://doi.org/10.1016/j.ijpx.2025.100361.

(11) Kawawaki, T.; Negishi, Y. Gold Nanoclusters as Electrocatalysts for Energy Conversion. *Nanomaterials*. 2020, p 238. https://doi.org/10.3390/nano10020238.

(12) Loynachan, C. N.; Soleimany, A. P.; Dudani, J. S.; Lin, Y.; Najer, A.; Bekdemir, A.; Chen, Q.; Bhatia, S. N.; Stevens, M. M. Renal Clearable Catalytic Gold Nanoclusters for in Vivo Disease Monitoring. *Nat. Nanotechnol.* **2019**, *14* (9), 883–890. https://doi.org/10.1038/s41565-019-0527-6.

(13) Cheng, D.; Liu, R.; Hu, K. Gold Nanoclusters: Photophysical Properties and Photocatalytic Applications. *Front. Chem.* **2022**, *Volume 10-2022*.

(14) Govindarajan, N.; Kastlunger, G.; Heenen, H. H.; Chan, K. Improving the Intrinsic Activity of Electrocatalysts for Sustainable Energy Conversion: Where Are We and Where Can We Go? *Chem. Sci.* **2022**, *13* (1), 14–26. https://doi.org/10.1039/D1SC04775B.

(15) Masa, J.; Andronescu, C.; Schuhmann, W. Electrocatalysis as the Nexus for Sustainable Renewable Energy: The Gordian Knot of Activity, Stability, and Selectivity. *Angew. Chemie Int. Ed.* **2020**, *59* (36), 15298–15312. https://doi.org/https://doi.org/10.1002/anie.202007672.

(16) Zhu, Q.; Gu, Y.; Wang, X.; Zhang, C.; Ma, J. Discovery of Electronic Structure and Interfacial Interaction Features in Catalytic Activity. *Langmuir* **2022**, *38* (13), 3959–3968. https://doi.org/10.1021/acs.langmuir.2c00176.

(17) den Boer, D.; Hetterscheid, D. G. H. Correlations between the Electronic Structure and Energetics of the Catalytic Steps in Homogeneous Water Oxidation Catalysis. *J. Am. Chem. Soc.* **2023**, *145* (42), 23057–23067. https://doi.org/10.1021/jacs.3c05741.

(18) Murillo-Gelvez, J.; Hickey, K. P.; Di Toro, D. M.; Allen, H. E.; Carbonaro, R. F.; Chiu, P. C. Experimental Validation of Hydrogen Atom Transfer Gibbs Free Energy as a Predictor of Nitroaromatic Reduction Rate Constants. *Environ. Sci. Technol.* **2019**, *53* (10), 5816–5827. https://doi.org/10.1021/acs.est.9b00910.

(19) Liu, Z.; Sardar, A.; Chen, S.; Wang, Y.; Jin, R. Atomically Precise Metal Nanoclusters for Near-Infrared-II Photonics. *Acc. Chem. Res.* **2026**, *59* (3), 451–463. https://doi.org/10.1021/acs.accounts.5c00782.

(20) Chen, Y.; Montana, D. M.; Wei, H.; Cordero, J. M.; Schneider, M.; Le Guével, X.; Chen, O.; Bruns, O. T.; Bawendi, M. G. Shortwave Infrared in Vivo Imaging with Gold Nanoclusters. *Nano Lett.* **2017**, *17* (10), 6330–6334. https://doi.org/10.1021/acs.nanolett.7b03070.

(21) Liu, H.; Hong, G.; Luo, Z.; Chen, J.; Chang, J.; Gong, M.; He, H.; Yang, J.; Yuan, X.; Li, L.; Mu, X.; Wang, J.; Mi, W.; Luo, J.; Xie, J.; Zhang, X.-D. Atomic-Precision Gold Clusters for NIR-II Imaging. *Adv. Mater.* **2019**, *31* (46), 1901015. https://doi.org/https://doi.org/10.1002/adma.201901015.

(22) Wang, W.; Kong, Y.; Jiang, J.; Xie, Q.; Huang, Y.; Li, G.; Wu, D.; Zheng, H.; Gao, M.; Xu, S.; Pan, Y.; Li, W.; Ma, R.; Wu, M. X.; Li, X.; Zuilhof, H.; Cai, X.; Li, R. Engineering the Protein Corona Structure on Gold Nanoclusters Enables Red-Shifted Emissions in the Second Near-Infrared Window for Gastrointestinal Imaging. *Angew. Chemie Int. Ed.* **2020**, *59* (50), 22431–22435. https://doi.org/https://doi.org/10.1002/anie.202010089.

(23) Ding, J.; Zhao, M.; Li, Y.; Zhang, K.; Chen, H.; Hu, X.; Li, L.; Su, Y.; Yuan, X.; Lin, Z. Atomically Precise Gold Nanoclusters as ROS-Scavenging Clusterzymes to Treat High-Fat Diet-Induced Obesity. *Chem. Eng. J.* **2024**, *496*, 153726.

(24) Yang, Y.; Yu, Y.; Chen, H.; Meng, X.; Ma, W.; Yu, M.; Li, Z.; Li, C.; Liu, H.; Zhang, X. Illuminating Platinum Transportation While Maximizing Therapeutic Efficacy by Gold Nanoclusters via Simultaneous Near-Infrared-I/II Imaging and Glutathione Scavenging. *ACS Nano* **2020**, *14* (10), 13536–13547.

(25) Wang, L.; Zhu, B.; Deng, Y.; Li, T.; Tian, Q.; Yuan, Z.; Ma, L.; Cheng, C.; Guo, Q.; Qiu, L. Biocatalytic and Antioxidant Nanostructures for ROS Scavenging and Biotherapeutics. *Adv. Funct. Mater.* **2021**, *31* (31), 2101804.

(26) Ye, C.; Zhang, D.-S.; Chen, B.; Tung, C.-H.; Wu, L.-Z. Interfacial Charge Transfer Regulates Photoredox Catalysis. *ACS Cent. Sci.* **2024**, *10* (3), 529–542. https://doi.org/10.1021/acscentsci.3c01561.

(27) Das, A.; Hessin, C.; Ren, Y.; Desage-El Murr, M. Biological Concepts for Catalysis and Reactivity: Empowering Bioinspiration. *Chem. Soc. Rev.* **2020**, *49* (23), 8840–8867. https://doi.org/10.1039/D0CS00914H.

(28) Verma, P.; Singh, A.; Rahimi, F. A.; Sarkar, P.; Nath, S.; Pati, S. K.; Maji, T. K. Charge-Transfer Regulated Visible Light Driven Photocatalytic H2 Production and CO2 Reduction in Tetrathiafulvalene Based Coordination Polymer Gel. *Nat. Commun.* **2021**, *12* (1), 7313. https://doi.org/10.1038/s41467-021-27457-4.

(29) Yu, M.; Ye, Z.; Liu, S.; Zhu, Y.; Niu, X.; Wang, J.; Ao, R.; Huang, H.; Cai, H.; Liu, Y.; Chen, X.; Lin, L. Redox-Active Ferrocene Quencher-Based Supramolecular Nanomedicine for NIR-II Fluorescence-Monitored Chemodynamic Therapy. *Angew. Chemie Int. Ed.* **2024**, *63* (10), e202318155. https://doi.org/https://doi.org/10.1002/anie.202318155.

(30) Yang, G.; Pan, X.; Feng, W.; Yao, Q.; Jiang, F.; Du, F.; Zhou, X.; Xie, J.; Yuan, X. Engineering Au44 Nanoclusters for NIR-II Luminescence Imaging-Guided Photoactivatable Cancer Immunotherapy. *ACS Nano* **2023**, *17* (16), 15605–15614. https://doi.org/10.1021/acsnano.3c02370.

(31) Guo, M.; Zhang, G.; Zhao, R.; Ma, H.; Yan, Y.; Yang, S.; Meng, J.; Huang, Y.; Zhang, X.-D.; Wang, H.; Zhang, R. Ligand Engineering of Gold Nanoclusters for NIR-II Imaging. *ACS Appl. Nano Mater.* **2023**, *6* (17), 15945–15958. https://doi.org/10.1021/acsanm.3c02888.

(32) Baek, G.; Pandurangan, P.; Ko, E.; Mo, Y.; Lee, D. Redox-Active Gold Nanoclusters Immobilized ZnO Nanorod Electrodes for Electrochemical Sensing Applications. *RSC Adv.* **2014**, *4* (21), 10766–10769. https://doi.org/10.1039/C4RA00256C.

(33) Kawawaki, T.; Negishi, Y. Elucidation of the Electronic Structures of Thiolate-Protected Gold Nanoclusters by Electrochemical Measurements. *Dalt. Trans.* **2023**, *52* (42), 15152–15167. https://doi.org/10.1039/D3DT02005C.

(34) El-Sayed, N.; Schneider, M. Advances in Biomedical and Pharmaceutical Applications of Protein-Stabilized Gold Nanoclusters. *J. Mater. Chem. B* **2020**, *8* (39), 8952–8971. https://doi.org/10.1039/D0TB01610A.

(35) Kumar, P. P.; Lim, D.-K. Gold-Polymer Nanocomposites for Future Therapeutic and

Tissue Engineering Applications. *Pharmaceutics*. 2022, p 70. https://doi.org/10.3390/pharmaceutics14010070.

(36) Saa, L.; Núñez-Martínez, M.; Carpintero-Cueto, E.; Cortajarena, A. L. Biomolecular Ligands as Tools to Modulate the Optical and Chiroptical Properties of Gold Nanoclusters. *Nanoscale* **2025**, *17* (7), 3671–3687. https://doi.org/10.1039/D4NR04267K.

(37) Hatakeyama-Sato, K.; Igarashi, Y.; Oyaizu, K. Charge-Transport Kinetics of Dissolved Redox-Active Polymers for Rational Design of Flow Batteries. *RSC Adv.* **2023**, *13* (1), 547–557. https://doi.org/10.1039/D2RA07208D.

(38) Biswas, S.; Shingyouchi, Y.; Kamiyama, M.; Jena, M. K.; Ogami, M.; Kawawaki, T.; Pathak, B.; Negishi, Y. Deciphering Electrocatalytic Activity in Cu Nanoclusters: Interplay Between Structural Confinement and Ligands Environment. *Small* **2025**, *21* (25), 2500302. https://doi.org/https://doi.org/10.1002/smll.202500302.

(39) Shan, H.; Shi, J.; Chen, T.; Cao, Y.; Yao, Q.; An, H.; Yang, Z.; Wu, Z.; Jiang, Z.; Xie, J. Modulating Catalytic Activity and Stability of Atomically Precise Gold Nanoclusters as Peroxidase Mimics via Ligand Engineering. *ACS Nano* **2023**, *17* (3), 2368–2377. https://doi.org/10.1021/acsnano.2c09238.

(40) Yan, Q.; Yuan, Z.; Wu, Y.; Zhou, C.; Dai, Y.; Wan, X.; Yang, D.; Liu, X.; Xue, N.; Zhu, Y.; Yang, Y. Atomically Precise Water-Soluble Gold Nanoclusters: Synthesis and Biomedical Application. *Precis. Chem.* **2023**, *1* (8), 468–479. https://doi.org/10.1021/prechem.3c00036.

(41) Hoque, M. E.; Bisht, R.; Unnikrishnan, A.; Dey, S.; Mahamudul Hassan, M. M.; Guria, S.; Rai, R. N.; Sunoj, R. B.; Chattopadhyay, B. Iridium-Catalyzed Ligand-Controlled Remote Para-Selective C−H Activation and Borylation of Twisted Aromatic Amides. *Angew. Chemie Int. Ed.* **2022**, *61* (27), e202203539. https://doi.org/https://doi.org/10.1002/anie.202203539.

(42) Zhang, K.; Peng, L.-Y.; Liu, X.-X.; Xu, X.; Fang, W.-H.; Cui, G.; Chen, Y.-Z.; Tung, C.-H.; Wu, L.-Z. Aromatic Amides: A Smart Backbone toward Isolated Ultralong Bright Blue-Phosphorescence in Confined Polymeric Films. *Angew. Chemie Int. Ed.* **2023**, *62* (22), e202300927. https://doi.org/https://doi.org/10.1002/anie.202300927.

(43) Podolak, M.; Holota, S.; Deyak, Y.; Dziduch, K.; Dudchak, R.; Wujec, M.; Bielawski, K.; Lesyk, R.; Bielawska, A. Tubulin Inhibitors. Selected Scaffolds and Main Trends in the Design of Novel Anticancer and Antiparasitic Agents. *Bioorg. Chem.* **2024**, *143*, 107076. https://doi.org/https://doi.org/10.1016/j.bioorg.2023.107076.

(44) Vogel, Y. B.; Stam, M.; Mulder, J. T.; Houtepen, A. J. Long-Range Charge Transport via Redox Ligands in Quantum Dot Assemblies. *ACS Nano* **2022**, *16* (12), 21216–21224. https://doi.org/10.1021/acsnano.2c09192.

(45) Nakada, A.; Matsumoto, T.; Chang, H.-C. Redox-Active Ligands for Chemical, Electrochemical, and Photochemical Molecular Conversions. *Coord. Chem. Rev.* **2022**, *473*, 214804. https://doi.org/https://doi.org/10.1016/j.ccr.2022.214804.

(46) Borca, B.; Michnowicz, T.; Aguilar-Galindo, F.; Pétuya, R.; Pristl, M.; Schendel, V.; Pentegov, I.; Kraft, U.; Klauk, H.; Wahl, P.; Arnau, A.; Schlickum, U. Chiral and Catalytic Effects of Site-Specific Molecular Adsorption. *J. Phys. Chem. Lett.* **2023**, *14* (8), 2072–2077. https://doi.org/10.1021/acs.jpclett.2c03575.

(47) Shangguan, H.; Fu, T.; Shen, C.; Hu, A.; Lin, H.; Liu, Z.; Zhang, C. Review on Fundamental and Recent Advances of Chiral Electrocatalysis for Efficient and Sustainable Energy Conversion. *Coord. Chem. Rev.* **2026**, *550*, 217395. https://doi.org/https://doi.org/10.1016/j.ccr.2025.217395.

(48) Zhao, X.; Zang, S.-Q.; Chen, X. Stereospecific Interactions between Chiral Inorganic Nanomaterials and Biological Systems. *Chem. Soc. Rev.* **2020**, *49* (8), 2481–2503. https://doi.org/10.1039/D0CS00093K.

(49) Liu, J.; Huang, X.; Li, Z.; Zhang, X.; Feng, Y.; Yuan, Z.; Gao, S.; El-Mesery, H. S.; Shi, J.; Zou, X. Chiral Engineering: Molecular Recognition to Macroscopic Assembly Dynamics. *Small* **2025**, *21* (47), e10195. https://doi.org/https://doi.org/10.1002/smll.202510195.

(50) Xiong, W.; Huang, Y.; Zhao, C.; Luo, Q.; Zhao, L.; Yu, F.; Cheng, Z. Engineering Ultrasmall Gold Nanoclusters: Tailored Optical Modulation for Phototherapeutic and Multimodal Biomedical Applications. *Chem. Commun.* **2025**, *61* (45), 8120–8136. https://doi.org/10.1039/D5CC02027A.

(51) Zhang, C.; Gao, X.; Chen, W.; He, M.; Yu, Y.; Gao, G.; Sun, T. Advances of Gold

Nanoclusters for Bioimaging. *iScience* **2022**, *25* (10). https://doi.org/10.1016/j.isci.2022.105022.

(52) Elbourne, A.; Coyle, V. E.; Truong, V. K.; Sabri, Y. M.; Kandjani, A. E.; Bhargava, S. K.; Ivanova, E. P.; Crawford, R. J. Multi-Directional Electrodeposited Gold Nanospikes for Antibacterial Surface Applications. *Nanoscale Adv.* **2019**, *1* (1), 203–212. https://doi.org/10.1039/C8NA00124C.

(53) Anshori, I.; Althof, R. R.; Rizalputri, L. N.; Ariasena, E.; Handayani, M.; Pradana, A.; Akbar, M. R.; Syamsunarno, M. R.; Purwidyantri, A.; Prabowo, B. A.; Annas, M. S.; Munawar, H.; Yuliarto, B. Gold Nanospikes Formation on Screen-Printed Carbon Electrode through Electrodeposition Method for Non-Enzymatic Electrochemical Sensor. *Metals*. 2022, p 2116. https://doi.org/10.3390/met12122116.

(54) Monti, M.; Brancolini, G.; Coccia, E.; Toffoli, D.; Fortunelli, A.; Corni, S.; Aschi, M.; Stener, M. The Conformational Dynamics of the Ligands Determines the Electronic Circular Dichroism of the Chiral Au38(SC2H4Ph)24 Cluster. *J. Phys. Chem. Lett.* **2023**, *14* (7), 1941–1948. https://doi.org/10.1021/acs.jpclett.2c03923.

(55) Yao, Y.; Ugras, T. J.; Meyer, T.; Dykes, M.; Wang, D.; Arbe, A.; Bals, S.; Kahr, B.; Robinson, R. D. Extracting Pure Circular Dichroism from Hierarchically Structured CdS Magic Cluster Films. *ACS Nano* **2022**, *16* (12), 20457–20469. https://doi.org/10.1021/acsnano.2c06730.

(56) Han, H.; Kallakuri, S.; Yao, Y.; Williamson, C. B.; Nevers, D. R.; Savitzky, B. H.; Skye, R. S.; Xu, M.; Voznyy, O.; Dshemuchadse, J.; Kourkoutis, L. F.; Weinstein, S. J.; Hanrath, T.; Robinson, R. D. Multiscale Hierarchical Structures from a Nanocluster Mesophase. *Nat. Mater.* **2022**, *21* (5), 518–525. https://doi.org/10.1038/s41563-022-01223-3.

(57) Kasha, M. Molecular Excitons in Small Aggregates. In *Spectroscopy of the excited state*; Springer, 1976; pp 337–363.

(58) Scholes, G. D.; Rumbles, G. Excitons in Nanoscale Systems. *Nat. Mater.* **2006**, *5* (9), 683–696.

(59) Puri, M.; Ferry, V. E. Circular Dichroism of CdSe Nanocrystals Bound by Chiral Carboxylic Acids. *ACS Nano* **2017**, *11* (12), 12240–12246.

(60) Ugras, T. J.; Carson, R. B.; Lynch, R. P.; Li, H.; Yao, Y.; Cupellini, L.; Page, K. A.; Wang, D.; Arbe, A.; Bals, S. Transforming Achiral Semiconductors into Chiral Domains with Exceptional Circular Dichroism. *Science (80-.).* **2025**, *387* (6733), eado7201.

(61) Zhou, M.; Jin, R.; Sfeir, M. Y.; Chen, Y.; Song, Y.; Jin, R. Electron Localization in Rod-Shaped Triicosahedral Gold Nanocluster. *Proc. Natl. Acad. Sci.* **2017**, *114* (24), E4697–E4705.

(62) Jo, H. H.; Lin, C.-Y.; Anslyn, E. V. Rapid Optical Methods for Enantiomeric Excess Analysis: From Enantioselective Indicator Displacement Assays to Exciton-Coupled Circular Dichroism. *Acc. Chem. Res.* **2014**, *47* (7), 2212–2221.

(63) Vasa, P.; Lienau, C. Strong Light–Matter Interaction in Quantum Emitter/Metal Hybrid Nanostructures. *Acs Photonics* **2018**, *5* (1), 2–23.

(64) Dolamic, I.; Knoppe, S.; Dass, A.; Bürgi, T. First Enantioseparation and Circular Dichroism Spectra of Au38 Clusters Protected by Achiral Ligands. *Nat. Commun.* **2012**, *3* (1), 798.

(65) Knoppe, S.; Bürgi, T. Chirality in Thiolate-Protected Gold Clusters. *Acc. Chem. Res.* **2014**, *47* (4), 1318–1326. https://doi.org/10.1021/ar400295d.

(66) Higaki, T.; Russell, J. C.; Paley, D. W.; Roy, X.; Jin, R. Electron Transport through Supercrystals of Atomically Precise Gold Nanoclusters: A Thermal Bi-Stability Effect. *Chem. Sci.* **2023**, *14* (45), 13191–13197.

(67) Ji, S.; Peng, D.; Sun, F.; You, Q.; Wang, R.; Yan, N.; Zhou, Y.; Wang, W.; Tang, Q.; Xia, N. Coexistent, Competing Tunnelling, and Hopping Charge Transport in Compressed Metal Nanocluster Crystals. *J. Am. Chem. Soc.* **2023**, *145* (44), 24012–24020.

(68) Mott, N. F.; Davis, E. A. *Electronic Processes in Non-Crystalline Materials*; OUP Oxford, 2012.

(69) Friedman, L.; Pollak, M. Hall Mobility Due to Hopping-Type Conduction in Disordered Systems. *Philos. Mag. B* **1978**, *38* (2), 173–189.

(70) Tokumoto, H.; Mansfield, R.; Lea, M. J. Hopping Conduction in N-Type Indium Antimonide below 1 K. *Philos. Mag. B* **1982**, *46* (2), 93–113.

(71) Shklovskii, B. I. Positive Magnetoresistance in the Variable-Range Hopping Region. *Sov. physics. Semicond.* **1983**, *17* (11), 1311–1316.

(72) Efros, A. L. On the Theory of Ac Conduction in Amorphous Semiconductors and Chalcogenide Glasses. *Philos. Mag. B* **1981**, *43* (5), 829–838.

(73) Azimzadeh Sani, M.; Pavlopoulos, N. G.; Pezzotti, S.; Serva, A.; Cignoni, P.; Linnemann, J.; Salanne, M.; Gaigeot, M.-P.; Tschulik, K. Unexpectedly High Capacitance of the Metal Nanoparticle/Water Interface: Molecular-Level Insights into the Electrical Double Layer. *Angew. Chemie Int. Ed.* **2022**, *61* (5), e202112679. https://doi.org/https://doi.org/10.1002/anie.202112679.

(74) Elliott, S. R. Ac Conduction in Amorphous Chalcogenide and Pnictide Semiconductors. *Adv. Phys.* **1987**, *36* (2), 135–217.

(75) Long, A. R. Frequency-Dependent Loss in Amorphous Semiconductors. *Adv. Phys.* **1982**, *31* (5), 553–637.

(76) Chen, F.; Mostafiz, B.; Suni, J.; Peltola, E. Electrochemical Design of Gold Nanostructures for Controllable Electrochemical Performance and Scalable Aptamer Sensing Application. *ACS Appl. Nano Mater.* **2025**, *8* (19), 9812–9823. https://doi.org/10.1021/acsanm.5c00962.

Supplementary Files

This is a list of supplementary files associated with this preprint. Click to download.

- SupportingInformationfile.pdf